

1 **The surface energy balance in a cold-arid permafrost environment, Ladakh**

2 **Himalaya, India**

3 John Mohd Wani¹, Renoj J. Thayyen^{2*}, Chandra Shekhar Prasad Ojha¹, and Stephan Gruber³

4 ¹Department of Civil Engineering, Indian Institute of Technology (IIT) Roorkee, India, ²Water

5 Resources System Division, National Institute of Hydrology, Roorkee, India

6 (renoj.nihr@gov.in; renojthayyen@gmail.com), ³Department of Geography & Environmental

7 Studies, Carleton University, Ottawa, Canada

8 **Abstract**

9 ~~The Recent studies have shown~~ cold-arid trans-Himalayan region comprises significant areas
10 underlain by permafrost. While the information on the permafrost characteristics ~~and extent of~~
11 ~~this region~~ started emerging, the governing energy regime ~~iss of this cryosphere region is~~ of
12 particular interest. This paper presents the results of ~~a~~ Surface Energy Balance (SEB) study
13 carried out in the upper Ganglass catchment in the Ladakh region of India, which feed directly
14 to the River Indus. The point-~~scale~~ SEB is estimated using the one-dimensional mode of
15 GEOTop model ~~from for the period of~~ 1 September 2015 to 31 August 2017 at 4727 m a.s.l
16 elevation. The model is evaluated using field monitored snow depth variations (accumulation
17 and melting), outgoing longwave radiation and ~~one-year~~ near-surface ground temperatures and
18 showed good agreement with the respective simulated values. For the study period, the ~~surface~~
19 ~~energy balance~~SEB characteristics of the study site show that the net radiation (29.7 W m⁻²)
20 was the major component, followed by sensible heat flux (-15.6 W m⁻²), latent heat flux (-11.2
21 W m⁻²) and ~~the~~ ground heat flux (~~was equal to~~ -0.5 W m⁻²). During both ~~the~~ years, the latent
22 heat flux was highest in summer and lowest in winter, whereas the sensible heat flux was
23 highest in post-winter and gradually decreased towards the pre-winter season. During the study
24 period, snow cover builds up ~~in the catchment initiated~~ ~~starting around~~ ~~by~~ the last week of

25 December, facilitating ~~the~~ ground cooling ~~by~~ during almost three months (October to
26 December) ~~of~~ with sub-zero temperatures ~~up~~ down to -20 °C providing a favourable
27 environment for permafrost. It is observed that the Ladakh region ~~have~~ has a very low relative
28 humidity in the range of 43% as compared to, e.g., ~70% in the European Alps, ~~facilitating~~
29 resulting in lower incoming longwave radiation and strongly negative net longwave radiation
30 averaging ~ -90 W m⁻² compared to -40 W m⁻² in the European Alps. Hence, ~~the land surfaces~~
31 at high elevation in cold-arid regions ~~land surfaces~~ could be overall colder than the locations
32 with ~~more RH~~ higher relative humidity, such as the European Alps. Further, it is apprehended
33 that high incoming shortwave radiation ~~in the region~~ during summer months in the region may
34 be facilitating enhanced cooling of wet valley bottom surfaces as a result of stronger
35 evaporation.

36 **Keywords:** Cold-arid, Cryosphere, GEOTop, Himalaya, Leh, Permafrost, Surface Energy
37 Balance

38 **1 Introduction**

39 The Himalayan cryosphere is essential for sustaining the flows in the major rivers originating
40 from the region (Bolch et al., 2012, 2019; Hock et al., 2019; Immerzeel et al., 2012; Kaser et
41 al., 2010; Lutz et al., 2014; Pritchard, 2019). These rivers flow through the most populous
42 regions of the world (Pritchard, 2019), and insight ~~on~~ into the processes driving ~~the future~~
43 change is critical for evaluating the future trajectory of water resources of the area, ranging
44 from small headwater catchments to large river systems (Lutz et al., 2014). It is hard to propose
45 a uniform framework for the downstream response of these rivers as they originate and flow
46 through various glacio-hydrological regimes of the Himalaya (Kaser et al., 2010; Thayyen and
47 Gergan, 2010). Lack of understanding of multiple processes driving the cryospheric response
48 of the region is limiting our ability to anticipate the subsequent changes and their impacts
49 correctly. This has been highlighted by ~~the~~ recent studies, which suggested the occurrence of

50 higher precipitation in the accumulation zones of the glaciers than previously known
51 (Bhutiyani, 1999; Immerzeel et al., 2015; Thayyen, 2020).

52 The sensitivity of mountain permafrost to climate change (Haeberli et al., 2010) leads to
53 changes in permafrost conditions such as an increase in active layer thickness that eventually
54 may affect the ground stability (Gruber and Haeberli, 2007; Salzmann et al., 2007), trigger
55 debris flows and rockfalls (Gruber et al., 2004; Gruber and Haeberli, 2007; Harris et al., 2001),
56 hydrological changes (Woo et al., 2008), run-off patterns (Gao et al., 2018; Wang et al., 2017),
57 water quality (Roberts et al., 2017), greenhouse gas emissions (Mu et al., 2018), alpine
58 ecosystem changes (Wang et al., 2006), and unique construction requirements to negate the
59 effects caused by ground-ice degradation (Bommer et al., 2010). These impacts strongly affect
60 ~~the~~ mountain communities and indicate the relevance of mountain permafrost on human
61 livelihoods. Field observations suggest that ground ice melt may be a critical water source in
62 dry summer years in the cold arid regions of Ladakh (Thayyen, 2015).

63 The energy balance at the earth's surface drives the spatio-temporal variability of ground
64 temperature (Oke, 2002; Sellers, 1965; Westermann et al., 2009). It is linked to the atmospheric
65 boundary layer, and location-dependent transfer mechanisms between land and the overlying
66 atmosphere (Endrizzi, 2007; Martin and Lejeune, 1998; McBean and Miyake, 1972). The
67 surface energy balance (SEB) in cold regions additionally depends on the seasonal snow cover,
68 vegetation and moisture availability in the soil (Lunardini, 1981) and (semi-) arid areas exhibit
69 their typical characteristics (Xia, 2010).

70 The role of permafrost is a key unknown variable in the Himalaya, especially in headwater
71 catchments of the Indus basin. ~~However, one can notice that the none of excellent studies about~~
72 ~~Himalayan cryosphere (e.g., Immerzeel et al., 2010; Lutz et al., 2014) discuss permafrost and~~
73 ~~its role in regional climate and Hydrology. And this is our prime motivation to take up the~~
74 ~~permafrost studies in the region.~~ A Recent recent studies study have has signalled significant

Formatted: Highlight

75 permafrost [area-occurrence](#) in the cold-arid [areas of upper-Upper Indus basin-Basin \(UIB\) areas](#)
76 covering Ladakh (Wani et al., 2020). ~~This study suggests that the permafrost area in a small~~
77 ~~(15.4 km²) catchment in the Ladakh region is 22 times of the glacier area. More coarse~~[Large-](#)
78 [scale](#) assessment in the Hindu Kush Himalaya (HKH) region suggests that the permafrost area
79 extends up to 1 million km², which roughly translate into 14 times the area of glacier cover of
80 the region (Gruber et al., 2017). Except for Bhutan, the expected permafrost areas in all other
81 countries [in the HKH region](#) is larger than the glacier area (cf. Table 1, Gruber et al., 2017).
82 ~~With two thirds of the HKH underlain by permafrost, China has by far the largest estimated~~
83 ~~share (906x10³ km²) followed by India (40.1x10³ km²), Pakistan (26.6x10³ km²), Afghanistan~~
84 ~~(17.5x10³ km²), Nepal (11.1x10³ km²), Bhutan (1.2x10³ km²) and Myanmar (0.1x10³ km²) (cf.~~
85 ~~Table 1, Gruber et al., 2017).~~

Formatted: Highlight

86 The mapping of rock glaciers using remote sensing suggested that the discontinuous permafrost
87 in the HKH region can be found between 3500 m a.s.l. in Northern Afghanistan to 5500 m a.s.l.
88 on the Tibetan Plateau (Schmid et al., 2015). [Recently, In the Indian Himalayan Region \(IHR\),](#)
89 [recent studies show that the discontinuous permafrost can be found between 3000-5500 m a.s.l.](#)
90 (Allen et al., 2016; Baral et al., 2019; Pandey, 2019). ~~Pandey (2019) published a remote sensing~~
91 ~~based rock glacier inventory of Himachal Himalaya and reports that the discontinuous~~
92 ~~permafrost can be found within an elevation range of 3000–5500 m a.s.l. Another rock glacier~~
93 ~~inventory from IHR suggests that the elevations above 4600 m a.s.l. are suitable for the~~
94 ~~occurrence of permafrost (Baral et al., 2019). Similarly, an initial localised estimate of 420 km²~~
95 ~~of permafrost is suggested in the Kullu district of Himachal Pradesh, India (Allen et al., 2016).~~

Formatted: Highlight

96 The cold-arid region of Ladakh has reported sporadic occurrence of permafrost and associated
97 landforms (Gruber et al., 2017; Wani et al., 2020) with ~~the~~ sorted patterned ground and other
98 periglacial landforms such as ice-cored moraines. [Field observations suggest that ground-ice](#)
99 [melt may also be a critical water source in dry summer years in the cold-arid regions of Ladakh](#)

100 [\(Thayyen, 2015\)](#). Previous studies of permafrost in the Ladakh region are from the Tso Kar
101 basin (Rastogi and Narayan, 1999; Wünnemann et al., 2008), and the Changla region (Ali et
102 al., 2018).

103 The SEB characteristics of different permafrost regions have been studied [in](#), e.g., the North
104 American Arctic (Eugster et al., 2000; Lynch et al., 1999; Ohmura, 1982, 1984), European
105 Arctic (Lloyd et al., 2001; Westermann et al., 2009), Tibetan Plateau (Gu et al., 2015; Hu et
106 al., 2019; Yao et al., 2008, 2011, 2020), European Alps (Mittaz et al., 2000) ~~or and~~ [Siberia](#)
107 (Boike et al., 2008; Kodama et al., 2007; Langer et al., 2011a, 2011b). However, SEB studies
108 of IHR are limited, for example, the energy balance studies on glaciers by Azam et al. (2014)
109 and Singh et al. (2020). [Besides its effect on heat transport into the subsurface, the SEB may](#)
110 ~~also has have~~ a significant influence on regional and local climate (Eugster et al., 2000). During
111 summer months, ~~the~~ permafrost creates a heat sink, which reduces the skin temperature, and
112 therefore [reduces](#) heat transfer to the atmosphere ~~is also reduced~~ (Eugster et al., 2000). This
113 highlight that the knowledge of frozen ground and associated energy regimes are a critical
114 knowledge gap in our understanding of the Himalayan cryospheric systems, especially in the
115 [Upper Indus Basin UIB](#).

116 The goal of this manuscript is to improve the understanding of permafrost in cold-arid UIB
117 areas and to advance our ability to analyse and simulate ~~the-its~~ [characteristics of permafrost](#)
118 ~~there~~. This can guide the application of available [permafrost](#) models in the Ladakh region,
119 which are calibrated (Boeckli et al., 2012) or validated (Cao et al., 2019; Fiddes et al., 2015)
120 elsewhere. Furthermore, it can help to interpret differences in surface offsets [\(difference](#)
121 [between the mean annual ground surface and mean annual air temperatures\)](#) observed in
122 Ladakh (Wani et al., 2020) and other permafrost areas (Boeckli et al., 2012; Hasler et al., 2015;
123 PERMOS, 2019). Our working hypothesis is that the surface offset for particular terrain types
124 in the UIB differs from what is known ~~in from~~ other areas, driven by aridity and high elevation.

125 We aim to improve the understanding of the SEB and its relationship with the ground
126 temperature by working on three objectives: (1) Quantifying the SEB at South Pullu, as an
127 ~~exemplar~~ example for permafrost areas in the UIB. (2) Understand the pronounced seasonal
128 and inter-annual variation of snowpack and GST, as these are intermediate phenomena between
129 the SEB and permafrost. (3) Understanding key differences with other permafrost areas that
130 have SEB observations.

131 2 Study area and data

132 2.1 Study area

133 The present study is carried out at South-Pullu (34.25°N, 77.62°E, 4727 m a.s.l.) in the upper
134 Ganglass catchment (34.25°N to 34.30°N and 77.50°E to 77.65°E), Leh, Ladakh (Figure 1).
135 Ladakh is a Union territory of India and has a unique climate, hydrology and landforms. Leh
136 is the district headquarter, where long-term climate data is available (Bhutiyani et al., 2007).
137 Long-term mean precipitation of Leh (1908-2017, 3526 m a.s.l.) is 115 mm (Lone et al.,
138 2019; Thayyen et al., 2013) and the daily minimum and maximum temperatures during the
139 period (2010 to 2012) range between -23.4 to 33.8 °C (Thayyen and Dimri, 2014). The spatial
140 area of the catchment is 15.4 km² and extends from 4700 m to 5700 m a.s.l. A small cirque
141 glacier called ~~as~~ Phuche glacier with an area of 0.62 km² occupies the higher elevations of the
142 catchment, ~~where a~~ A single stream originates and flows through the valley of the catchment
143 originating from Phuche glacier. This stream flows intermittently with ~~a~~ most of the maximum
144 mean daily flow (number here?) of 3.57 m³/s (in wet years) and 0.4 m³/s in (dry years)
145 during from ~~from~~ May to October period.

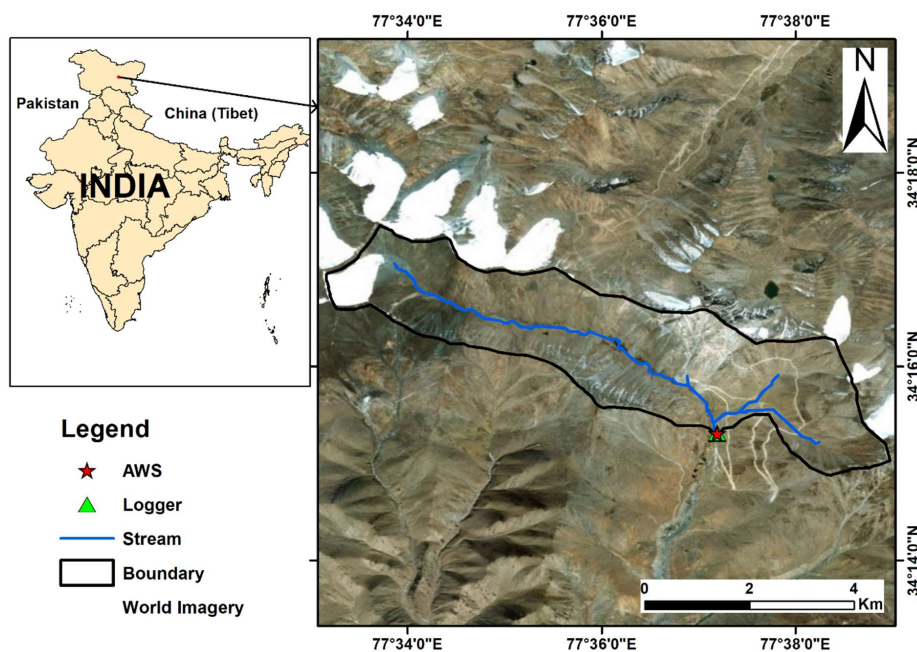
146 ~~The catchment lies in the Ladakh mountain range and~~ The catchment is part of the main Indus
147 river basin ~~and belongs to the~~ geologically unit of, ~~the study catchment is part of~~ the Ladakh
148 batholith (Thakur, 1981). The study catchment also consists of steep mountain slopes with the
149 valley bottom filled with glacio-fluvial deposits. Other sporadic landforms found in the

Formatted: Font color: Red

Formatted: Superscript

Formatted: Superscript

150 catchment include patterned ground, boulder fields, peatlands, high elevation wetlands and a
151 small lake. Many of these landforms point towards intense frost action in the area.



152
153 Figure 1 Location of the study site in the upper Ganglass catchment. (Base image sources on
154 the right panel: © Esri, DigitalGlobe, GeoEye, Earthstar Geographic's, CNES/Airbus DS,
155 USDA, USGS, AEX, Getmapping, Aerogrid, IGN, IGP, swisstopo, and the GIS User
156 Community).

157 2.2 Meteorological data used

158 The automatic weather station (AWS) in the catchment is located at an elevation of 4727 m
159 a.s.l. at South-Pullu (Figure 1). It is located in [the a wide southeast oriented](#) deglaciated valley
160 [trending southeast](#). The site has a local slope angle of 15°, and the soil is sparsely vegetated.
161 Weather data has been collected by a Sutron automatic weather station from 1 September 2015
162 to 31 August 2017. The study years 1 September 2015 to 31 August 2016 and 1 September
163 2016 to 31 August 2017 hereafter in the text will be designated as 2015-16 and 2016-17.

164 respectively. The variables measured include air temperature, relative humidity, wind speed
165 and direction, incoming and outgoing shortwave and longwave radiation and snow depth
166 (Table 1). The snow depth is measured using a Campbell SR50 sonic ranging sensor with a
167 nominal accuracy of ± 1 cm (Table 1). To reduce the noise of the measured snow depth, a six-
168 hour moving average is applied. Near-surface ground temperature (GST) is measured at a depth
169 of 0.1 m near the AWS using miniature temperature data logger (MTD) manufactured by
170 GeoPrecision GmbH, Germany. GST data was available only from 1 September 2016 to 31
171 August 2017 and is used for model evaluation only. All the four solar radiation components,
172 i.e., incoming shortwave (SW_{in}), outgoing shortwave (SW_{out}), incoming longwave (LW_{in}) and
173 outgoing longwave (LW_{out}) radiation were measured. Before using these data in the SEB
174 calculations, necessary corrections were applied (Nicholson et al., 2013; Oerlemans and Klok,
175 2002): (a) all the values of $SW_{in} < 5 \text{ Wm}^{-2}$ are set to zero, (b) when $SW_{out} > SW_{in}$ (3 % of data
176 under study), it indicates that the upward-looking sensor was covered with snow (Oerlemans
177 and Klok, 2002). The SW_{out} can be higher than SW_{in} at high elevation sites such as this one due
178 to high solar zenith angle during the morning and evening hours (Nicholson et al., 2013). In
179 such cases, SW_{in} was corrected by SW_{out} divided by the accumulated albedo, calculated by the
180 ratio of measured SW_{out} and measured SW_{in} for a 24h period (van den Broeke et al., 2004).

181
182
183
184
185
186
187
188

189

190 Table 1 Technical parameters of different sensors at South-Pullu (4727 m a.s.l.) in the upper

191 Ganglass catchment, Leh. (MF: model forcing, ME: model evaluation).

Variable	Units	Sensor	Stated accuracy	Height (m)	Use
Air temperature	(°C)	Rotronics-5600-0316-1	±0.2 °C	2.2	MF
Relative humidity	(%)	Rotronics-5600-0316-1	±1.5%	2.2	MF
Wind speed	(m s ⁻¹)	RM Young 05103-45	±0.3 ms ⁻¹	10	MF
Wind direction	(°)	RM Young 05103-45	±0.3°	10	MF
Incoming shortwave radiation	(W m ⁻²)	Kipp and Zonen (CMP6) (285 to 2800nm)	±10%	4.6	MF
Outgoing shortwave radiation	(W m ⁻²)	Kipp and Zonen (CMP6) (285 to 2800nm)	±10%	4.6	MF
Incoming longwave radiation	(W m ⁻²)	Kipp and Zonen (CGR3) (4500 to 42000nm)	±10%	4.3	MF
Outgoing longwave radiation	(W m ⁻²)	Kipp and Zonen (CGR3) (4500 to 42000nm)	±10%	4.3	ME
Snow depth	(m)	Campbell SR-50	±1cm	3.44	ME
Data logger	-	Sutron 9210-0000-2B	-	-	-
Near-surface ground temperature	(°C)	PT1000 in stainless steel cap (by GeoPrecision GmbH, Germany)	±0.1 °C	-0.1	ME

192

193 3 Methods

194 3.1 Estimation of precipitation from snow height

195 In high elevation and remote sites, the [snowfall](#) measurement [of snowfall](#) is a difficult task with
196 an under catch of 20–50% (Rasmussen et al., 2012; Yang et al., 1999). At the South Pullu
197 station, daily precipitation including snow was measured using a non-recording rain gauge. In
198 this high elevation area, an under catch of 23% of snowfall was reported earlier (Thayyen et
199 al., 2015) [Unpublished work]. [Here](#)[In this study, the total precipitation was recorded at daily](#)
200 [temporal resolution, whereas the we had the time resolution problem between total measured](#)
201 [precipitation and other meteorological forcing's including SR50 snow depth, were recorded at](#)
202 [\(hourly, time steps and recorded by automatic weather station\)](#). Therefore, to match the

Formatted: Not Highlight

203 temporal resolution of precipitation data with [the](#) other meteorological forcing [data's](#), we
 204 adopted the method proposed by Mair et al. (2016), called Estimating SOLid and Liquid
 205 Precipitation (ESOLIP). This method makes use of snow depth and meteorological
 206 observations to estimate the sub-daily solid precipitation in terms of snow water equivalent
 207 (SWE). In ESOLIP, we considered [daily](#) liquid precipitation [daily](#) only. The ESOLIP method
 208 consists of [the](#) following steps:

- 209 1. ~~(a) filtering~~ Filtering of precipitation readings ~~related to: simplified simple criteria~~
 210 ~~based on~~ relative humidity (RH) and global shortwave radiation ~~criteria was used such~~
 211 ~~as, for an actual precipitation event, (e.g., the~~ RH > 50% and SWin < 400 W m⁻²);
- 212 2. ~~(b) P~~precipitation type determination: wet bulb temperature (T_w) is used to differentiate
 213 between rain and snow, ~~i.e. rainfall assumed for such as if~~ $T_w < 1$ (SWE estimation)
 214 and if $T_w > 1$, ~~(rain). The~~ T_w is estimated by solving the psychrometric formula
 215 implicitly: $e = E(T_w) - \gamma(T_a - T_w)$, T_a is the air temperature, and e (hPa) is the
 216 vapour pressure in the air, E (hPa) is the saturation vapour pressure, and γ (hPa K⁻¹) is
 217 the ~~psychrometer~~ psychrometric constant depending on air pressure;
- 218 3. ~~(e) e~~Estimation of density: the fresh snow density (ρ) was estimated based on air
 219 temperature (T_a) and wind speed ~~measured at 10 m height~~ (u_{10}) as ~~below follows~~
 220 (Jordan et al., 1999):

$$\rho = 500 * [1 - 0.951 * \exp(-1.4 * (278.15 - T_a)^{-1.15} - 0.008u_{10}^{1.7})], \quad (1)$$

221 For $260.15 < T_a \leq 275.65$ K

$$\rho = 500 * [1 - 0.904 * \exp(-0.008u_{10}^{1.7})], \quad (2)$$

222 For $T_a \leq 260.15$ K

Formatted: Font

Formatted: List Paragraph, Numbered + Level: 1 + Numbering Style: 1, 2, 3, ... + Start at: 1 + Alignment: Left + Aligned at: 0.31" + Indent at: 0.56"

Formatted: Font

Formatted: Font

Formatted: Font

Formatted: Font

Formatted: Font

Formatted: Font

Formatted: Font

Formatted: Font (Default) Cambria Math

Formatted: Font (Default) Cambria Math

Formatted: Font (Default) Cambria Math

Formatted: Font (Default) Cambria Math

Formatted: Font (Default) Cambria Math

Formatted: List Paragraph

Formatted: Indent: Left: 0.31"

Formatted: List Paragraph, Left

Formatted Table

Formatted: Font (Default) Cambria Math

Formatted: Font (Default) Cambria Math

Formatted: Font (Default) Cambria Math

Formatted: Font (Default) Cambria Math

Formatted: Font (Default) Cambria Math

Formatted: Font

Formatted: List Paragraph, Centered

Formatted: Font (Default) Cambria Math

Formatted: Font (Default) Cambria Math

Formatted: Font (Default) Cambria Math

Formatted: Font (Default) Cambria Math

Formatted: Indent: Left: 0.31"

Formatted: List Paragraph, Left

Formatted Table

225 and

226 4. ~~(d)~~ Estimation of SWE ($SWE = h \cdot \rho$): to estimate the SWE of single snowfall events
227 using snow depth (h) measurements. ~~An~~ ~~and~~ identification of the snow height
228 increments of the single snowfall events and an accurate estimate of the snow density
229 are necessary.

230 3.2 Modelling of ~~point~~ surface energy balance

231 In this study, the open-source model GEOtop version 2.0 (hereafter GEOtop) (Endrizzi et al.,
232 2014; Rigon et al., 2006) was used for the modelling of point surface energy balance, including
233 the evolution of the snow depth and the transfer of heat and water in snow and soil. GEOtop
234 represents the combined ground heat and water balance, as well as the exchange of energy with
235 the atmosphere by taking into consideration the radiative and turbulent heat fluxes. The model
236 has a multi-layer snowpack and solves the energy and water balance of the snow cover and soil
237 including the highly non-linear interactions between the water and energy balance during soil
238 freezing and thawing (Dall'Amico et al., 2011). It can be applied in complex terrain and makes
239 it possible to account for topographical and other environmental variability (Fiddes et al., 2015;
240 Gubler et al., 2013).

241 Previous studies have successfully applied GEOtop in mountain regions, e.g., simulating snow
242 depth ~~and ground temperature~~ (Endrizzi et al., 2014), snow cover mapping (Dall'Amico et al.,
243 2011b, 2018; Engel et al., 2017; Zanotti et al., 2004), ecohydrological processes (Bertoldi et
244 al., 2010; Chiesa et al., 2014), modelling of ground temperatures in complex topography
245 (Bertoldi et al., 2010; Endrizzi et al., 2014; Fiddes and Gruber, 2012; Gubler et al., 2013), water
246 and energy fluxes (Hingerl et al., 2016; Rigon et al., 2006; Soltani et al., 2019),
247 evapotranspiration (Mauder et al., 2018), and permafrost distribution (Fiddes et al., 2015) ~~or~~
248 ~~modelling ground temperatures (Bertoldi et al., 2010; Gubler et al., 2013).~~

Formatted: Left

Formatted: List Paragraph, Numbered + Level: 1 +
Numbering Style: 1, 2, 3, ... + Start at: 1 + Alignment:
Left + Aligned at: 0.31" + Indent at: 0.56"

Formatted: Font: Italic

249 Generally, the surface energy balance (SEB) (Eq. 3) is written as a combination of net radiation
250 (R_n), sensible (H) and latent heat (LE) flux and heat conduction into the ground or to the snow
251 (G) and must balance at all times (Oke, 2002):

252

$$R_n + H + LE + G - F_{surf} = 0 \quad (3)$$

253

254 where F_{surf} is the resulting latent heat flux in the snowpack due to melting or freezing. We use
255 the sign convention adopted in this study is as, that the energy fluxes towards the surface are
256 positive, and fluxes away from the surface are negative if directed away from the surface
257 (Mölg, 2004). During the summertime, when conditions for snow melting are prevailing at the
258 ground surface, the F_{surf} is negative (loss from the system) as a result of energy available for
259 melting snow and warming the ground under snow-free conditions. The positive F_{surf}
260 (gain to the system) during summertime is the energy released to refreeze the water and
261 represents the freezing flux.

262 In the cold regions, the SEB is a complex function of solar radiation, seasonal snow cover,
263 vegetation, near-surface moisture content, and atmospheric temperature (Lunardini, 1981).

264 Based on the available in-situ available data, the calculation of SEB components like H, LE
265 and G is difficult. For example, in the calculation of turbulent heat fluxes (H and LE), the wind
266 speed and temperature measurements near the ground surface are required at two heights,
267 which are generally not available. Therefore, parameterisation method, like the bulk
268 aerodynamic method, is used, which is valid under statically neutral conditions in the surface
269 layer (Stull, 1988). Hence, the application of a tested model like GEOtop (Endrizzi et al., 2014;
270 Rigon et al., 2006) is a good alternative for the estimation of these fluxes. In However, in the
271 GEOtop (Endrizzi et al., 2014), the general SEB equation of SEB (Eq. 3) is linked with the
272 water balance and is written as (Eq. 4):

273

$$F_{surf}(T_s) = SW_n + LW_n(T_s) + H(T_s) + LE(T_s, \theta_w) \quad (4)$$

274

275 where T_s , the temperature of the surface, is ~~an unknown in the equation~~, SW_n is the net
 276 shortwave radiation, LW_n is the net longwave radiation. ~~The F_{surf} is a function of the T_s . Other~~
 277 terms in Eq. 4 which are a function of T_s include LW_n , H and LE. In addition, ~~the LE also~~
 278 depends also on the soil moisture at the surface (θ_w), linking the SEB and water balance
 279 equations. The equations and the key elements of GEOTop are explained in Endrizzi et al.
 280 (2014); ~~and here, only a brief description of the equations that are of interest in this study is~~
 281 given. ~~The SW_n in Eq. 4 is equal to the difference between the incoming solar radiation (SW_{in})~~
 282 ~~coming from the atmosphere and the reflected shortwave radiation (SW_{out}) (Oke, 2002). Also,~~
 283 ~~LW_n in Eq. 4 is equal to the difference between the incoming longwave radiation (LW_{in})~~
 284 ~~coming from the atmosphere and the outgoing longwave radiation (LW_{out}) radiated by the~~
 285 ~~surface (Oke, 2002). The LW_{out} radiated by the surface is also estimated using the Stefan-~~
 286 Boltzmann law ~~(Eq. 5), as below:~~

287

$$LW_{out} = \epsilon_s \cdot \sigma \cdot T_s^4 \quad (5)$$

288

289 where ~~T_s is the surface temperature (K) and~~ ϵ_s is the surface emissivity.
 290 The turbulent fluxes (H and LE) are driven by the gradients of temperature and specific
 291 humidity between the air and the surface, and due to turbulence caused by winds as the primary
 292 transfer mechanism in the boundary layer (Endrizzi, 2007). GEOTop estimates the turbulent
 293 heat fluxes H (Eq. 6) and LE (Eq. 7) using the flux-gradient relationship (Brutsaert, 1975;
 294 Garratt, 1994) as below follows:

295

$$H = \rho_a c_p w_s \frac{T_a - T_s}{r_a} \quad (6)$$

$$LE = \beta_{YP} L_e \rho_a c_p w_s \frac{Q_a - \alpha_{YP} Q_s^*}{r_a} \quad (7)$$

296
 297 where ρ_a is the air density (kg m^{-3}), w_s is the wind speed (m s^{-1}), c_p the specific heat at constant
 298 pressure ($\text{J kg}^{-1} \text{K}^{-1}$), L_e the specific heat of vaporisation (J kg^{-1}), Q_a and Q_s^* are the specific
 299 humidity of the air (kg kg^{-1}) and saturated specific humidity at the surface (kg kg^{-1}),
 300 respectively, β_{YP} and α_{YP} are the coefficients that take into account the soil resistance to
 301 evaporation and only depend on the liquid water pressure close to the soil surface, and r_a is the
 302 aerodynamic resistance (-). The aerodynamic resistance is obtained applying the Monin–
 303 Obukhov similarity theory (Monin and Obukhov, 1954), which requires that values of wind
 304 speed, air temperature and specific humidity are available at least at two different heights above
 305 the surface. But the values of these variables are generally measured at a standard height above
 306 the surface and can be used for the near-ground surface with the following assumptions: (a) the
 307 air temperature is equal to the ground surface temperature; however, this assumption leads to
 308 the boundary condition nonlinearity, (b) the specific humidity is equal to $\alpha_{YP}Q_s^*$, and (c) wind
 309 speed is equal to zero.

310 The coefficients β_{YP} and α_{YP} are the coefficients (Eq. 8 and 9) that take into account the soil
 311 resistance to evaporation, and only depend on the liquid water pressure close to the soil surface.
 312 They are calculated according to the parameterisation of Ye and Pielke (1993), which considers
 313 evaporation as the sum of the proper evaporation from the surface and diffusion of water vapour
 314 in soil pores at greater depths:

$$315 \quad \beta_{YP} = \chi_p(g) - \frac{[\chi_p(g) - \theta_g]}{1 + \frac{\chi_p(1) - \theta(1)r_a}{\chi_p(g) - \theta_g r_d}} \quad (8)$$

$$317 \quad \alpha_{YP} = \frac{1}{\beta_{YP}} \left[\theta_g + \frac{\chi_p(1) - \theta(1)}{1 + \frac{\chi_p(1) - \theta(1)r_a}{\chi_p(g) - \theta_g r_d}} \frac{r_a}{r_d} h_s(\theta_1) \frac{q(T_s)_{sat}}{q(T_g)_{sat}} \right] \quad (9)$$

319 where q^{sat} is the specific humidity in the saturated condition, the subscripts g and l in above
320 two equations refer to the ground surface and a thin layer next to the ground surface,
321 respectively, θ is the volumetric water content of the soil, χ_p is the volumetric fraction of soil
322 pores, h_s is the relative humidity in the pores, T_g is the temperature at the ground surface, r_d is
323 the soil resistance to water vapour diffusion.

324 3.2.1 The heat equation and snow depth

325 The equation (Eq. 10) representing the energy balance in a soil volume subject to phase change
326 in GEOtop is given below (Endrizzi et al., 2014):

$$\frac{\partial U^{ph}}{\partial t} + \nabla \cdot \mathbf{G} + S_{en} - \rho_w [L_f + c_w(T - T_{ref})] S_w = 0 \quad (10)$$

327 where U^{ph} is the volumetric internal energy of soil ($J m^{-3}$) subject to phase change, t (s) is time,
328 ~~∇ the divergence operator,~~ G the heat conduction flux ($W m^{-2}$), S_{en} is the energy sink term
329 ($W m^{-3}$), S_w is the mass sink term (s^{-1}), L_f ($J kg^{-1}$) the latent heat of fusion, ρ_w the density of
330 liquid water in soil ($kg m^{-3}$), c_w is the specific thermal capacity of water ($J kg^{-1} K^{-1}$), T ($^{\circ}C$),
331 the soil temperature and T_{ref} ($^{\circ}C$) the reference temperature at which the internal energy is
332 calculated. If G is written according to Fourier's law, the Eq. 10 becomes:

$$\frac{\partial U^{ph}}{\partial t} + \nabla \cdot (\lambda_T \nabla T) + S_{en} - \rho_w [L_f + c_w(T - T_{ref})] S_w = 0 \quad (11)$$

334 where λ_T is the thermal conductivity ($W m^{-1} K^{-1}$), which is a non-linear
335 function of temperature, because the proportion of liquid water and ice contents depends on
336 temperature. For the calculation of λ_T , the GEOtop uses the method proposed by Cosenza et
337 al. (2003). The detailed description of the heat conduction equation used in GEOtop can be
338 found in Endrizzi et al. (2014).

340 The snow cover buffers the energy exchange between the soil and atmosphere and critically
341 influences the soil thermal regime (Endrizzi et al., 2014). GEOtop includes a multi-layer,

342 energy-based, Eulerian snow modelling approach with similar equations. ~~In GEOTop, the~~
343 ~~equations for snow modelling are similar~~ to the ones used for the soil matrix (Endrizzi et al.,
344 2014). The discretisation of snow in GEOTop is done ~~carried out in such a way so that these~~
345 ~~describe the~~ thermal gradients inside the snowpack are described accurately ~~which are~~ finer
346 ~~near the surface (with the atmosphere) and at the bottom (with soil). In GEOTop, t~~The effective
347 thermal conductivity at the interface of-between snow and ground is calculated similarly as ~~in~~
348 between different soil layers using the method of Cosenza et al. (2003). ~~In GEOTop, the f~~resh
349 snow density is computed using the Jordan et al. (1999) formula, which is based on air
350 temperature and wind speed. More details about the snow metamorphism compaction rates and
351 the snow discretisation in GEOTop can be found in the appendix D2 and D3 ~~, respectively~~ of
352 ~~(Endrizzi et al., (2014).~~

Formatted: Highlight

Formatted: Highlight

Field Code Changed

353 3.2.2 Model setup and forcing's

354 The 1D GEOTop simulation was carried out at South-Pullu (Figure 1). The soil column is 10 m
355 deep and is discretised into 19 layers, with thickness increasing from the surface to the deeper
356 layers. The top 8 layers close to the ground surface were resolved with thicknesses ranging
357 from 0.1 to 1 m, because of the higher temperature and water pressure gradients near the
358 surface. ~~(Endrizzi et al., 2014),~~ while the lowest layer is 4.0 m thick.

359 The snowpack is discretised in 10 layers, which are finer at the top at the interfaces with the
360 atmosphere and ~~the bottom with the~~ soil.

361 The model was initialised at-with a uniform soil temperature of -0.5 °C and spun up by
362 repeatedly modelling the soil temperature down to 1 m (2 years*25 times), and then using the
363 modelled soil temperatures as an initial condition to repeatedly simulate soil temperature down
364 to 10 m (2 years *25 times) (c.f., Fiddes et al., 2015; Gubler et al., 2013; Pogliotti, 2011).

365 Preliminary-Prior tests showed ed that the minimum number of repetitions required to bring the

366 soil column to equilibrium was 25 (Figure S1). The values of all the input parameters used [in](#)
367 [the study is are](#) given in [the](#) Appendix (Table A1 to A4) in the supplementary material.

368 The input meteorological data required for running the 1D GEOTop model include time series
369 of precipitation, air temperature, relative humidity, wind speed, wind direction and solar
370 radiation components and the description of the site (slope angle, elevation, aspect ~~angle~~, and
371 sky view factor) for the simulation point. The model was run at an hourly time step
372 corresponding to the measurement time step of the meteorological data.

373 3.3 Model performance evaluation

374 While the accuracy of simulated energy fluxes cannot be quantified, the quality of GEOTop
375 simulations is evaluated based on ~~proxy variables such as~~ snow depth, GST and ~~the~~ LW_{out}.
376 These variables were chosen because they have not been used to drive the model, and they
377 represent different physical processes affected by surface energy balance. ~~For example, (a)~~
378 ~~†~~The melt-out date of the snow depth is [hereby](#) a good indicator showing how good the surface
379 mass and energy balance is simulated, ~~whereas and (b) the~~ GST is the result of all the processes
380 occurring at the ground surface such as radiation, turbulence, latent and sensible heat fluxes
381 (Gubler, 2013), ~~and (c) LW_{out} which~~ is governed by the temperature and emissivity at the
382 surface, and ~~the~~ Eq. 3 is solved in terms of [the](#) skin temperature. Therefore, ~~the~~ LW_{out} is used
383 as a proxy for the evaluation of [the](#) SEB.

384 Model performance is evaluated based on the measured and the simulated time series, ~~(Gubler~~
385 ~~et al., 2012)~~. Typically, a variety of statistical measures are used to assess the model
386 performance because no single measure encloses all aspects of interest. In this study ~~also~~, R²
387 ~~(Carslaw and Ropkins, 2012)~~, mean bias difference (MBD) and the root mean square difference
388 (RMSD) ~~(Badescu et al., 2012; Gubler et al., 2012; Gueymard, 2012)~~, MB and RMSE ~~(Gupta~~
389 ~~et al., 1999)~~, and NSE (Nash and Sutcliffe, 1970) were used (Eq. S1 to S6).

390 4 Results

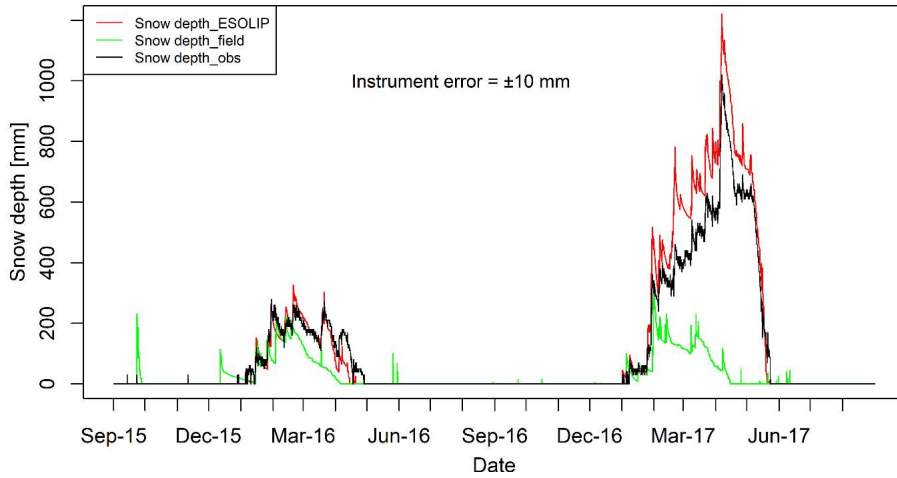
391 4.1 Model evaluation

392 In this section, the capability of GEOTop to reproduce ~~the proxy variables is evaluated. The~~
393 ~~model was evaluated based on~~ snow depth, ~~one-year~~ GST and ~~the~~ LW_{out}. ~~In this study, the~~
394 ~~simulation results are~~ based on ~~the~~ standard model parameters obtained from ~~the~~ literature
395 (Table 2 and 3, Gubler et al., 2013) ~~was evaluated, i.e. model results and~~ were not improved
396 by trial and error ~~and the same simulation results are used for model evaluation.~~

397 4.1.1 Evaluation of snowpack

398 Snow depth variations simulated by GEOTop are compared with observations from 1
399 September 2015 to 31 August 2017 (Figure 2). The model captures the peaks, start and melt-
400 out dates of the snowpack, as well as overall fluctuations ([Figure S2](#), $R^2 = 0.98$, RMSE = 59.5
401 mm, MB = 16.7 mm, NSE = 0.91, Instrument error = ± 10 mm) ~~(Figure S2)~~. The maximum
402 ~~standing simulated~~ snow height (h) ~~simulated by the GEOTop~~ was 1219 mm in comparison to
403 the 1020 mm measured in the field. In the low snow year ~~(2015-16)~~, the maximum simulated
404 h was 326 mm in comparison to ~~the~~ 280 mm measured in the field. During the melting period
405 of the low and high snow years, the snow depth was slightly under-estimated. However, during
406 the accumulation period of high snow year (2016-17), ~~the~~ h was rather overestimated by the
407 model.

408 ~~Furthermore, the~~ The performance of the ESOLIP estimated precipitation was evaluated against
409 a ~~controlled~~ run with precipitation data measured in the field (Figure 2). ESOLIP is the superior
410 approach for precipitation estimation, where snow depth and necessary meteorological
411 measurements are available.

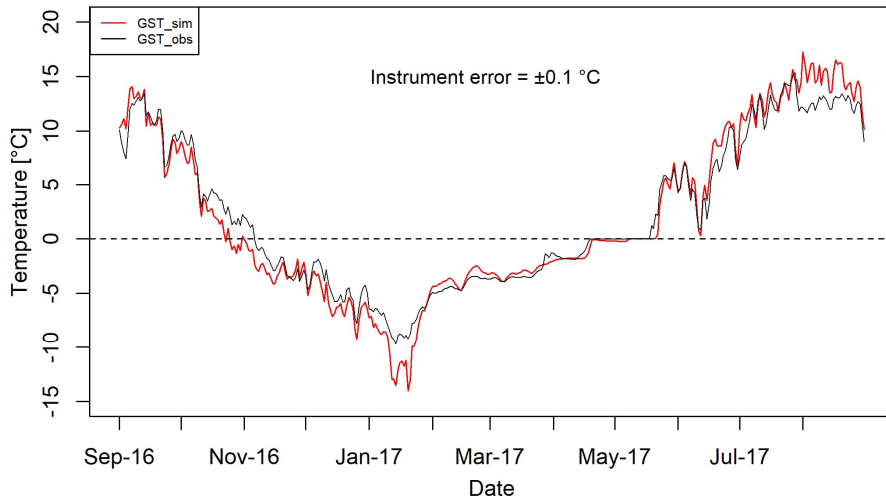


412

413 Figure 2 Comparison of hourly observed and GEOFtop simulated snow depth at South-Pullu
 414 (4727 m a.s.l.) from 1 September 2015 to 31 August 2017. The black line denotes the snow
 415 depth measured in the field by [the](#) SR50 sensor. The red (Snow depth_ESOLIP) and green
 416 (Snow depth_field) lines in the plot indicate the GEOFtop simulated snow depth based on
 417 ESOLIP estimated precipitation and precipitation measured in the field, respectively.

418 **4.1.2 Evaluation of near-surface ground temperatures (GST)**

419 GST is simulated (GST_sim) on an hourly basis and compared with the observed values
 420 (GST_obs) near the AWS, available from 1 September 2016 to 31 August 2017 (Figure 3). The
 421 results show a reasonably good linear agreement between the simulated and observed GSTs
 422 (Figure S3, $R^2 = 0.97$, MB = -0.11 °C, RMSE = 1.63 °C, NSE = 0.95, Instrument error = ±0.1
 423 °C). The model estimated the dampening of soil temperature fluctuations by the snowpack and
 424 the zero-curtain period at the end of melt-out of the snowpack reasonably well.



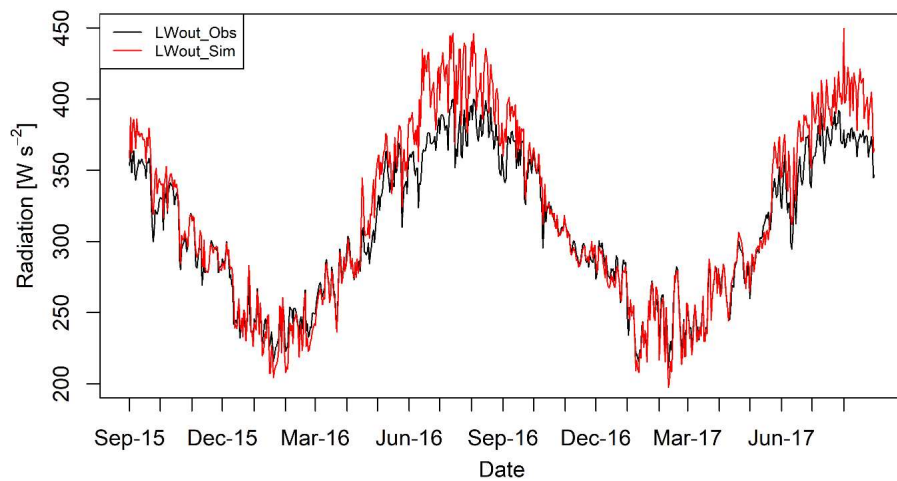
425

426 Figure 3 Comparison of daily mean observed (GST_obs, °C) and GEOTop simulated near-
 427 surface ground temperature (GST_sim, °C) at South-Pullu (4727 m a.s.l.) from 1 September
 428 2016 to 31 August 2017.

429 **4.1.3 Evaluation of outgoing longwave radiation**

430 Modelled LW_{out} is evaluated with the observed measurements and a comparison of daily mean
 431 observed, and simulated LW_{out} is shown in Figure 4. The daily mean LW_{out} matches very well
 432 with the observed data, except during summer months when the simulated LW_{out} was slightly
 433 overestimated than the observed values. The hourly LW_{out} shows a good linear relationship
 434 (Figure S4, R² = 0.93, NSE = 0.73) but the GEOTop slightly overestimates the LW_{out} (MBD =
 435 3 %) with RMSD value of 10 % (Instrument error = ±10%).

436 Based on the evaluation of LW_{out}, the GEOTop can simulate the surface temperature at the point
 437 scale; therefore, we believe that it can reasonably calculate the [different](#) SEB components.



438

439 Figure 4 Comparison of daily mean observed [outgoing longwave radiation](#) (LW_{out_obs}) and
 440 GEOTop simulated (LW_{out_sim}) [outgoing longwave radiation](#) -at South-Pullu (4727 m a.s.l.)
 441 from 1 September 2015 to 31 August 2017. The instrument error for the Kipp and Zonen
 442 (CGR3) (4500 to 42000nm) radiometer is $\pm 10\%$.

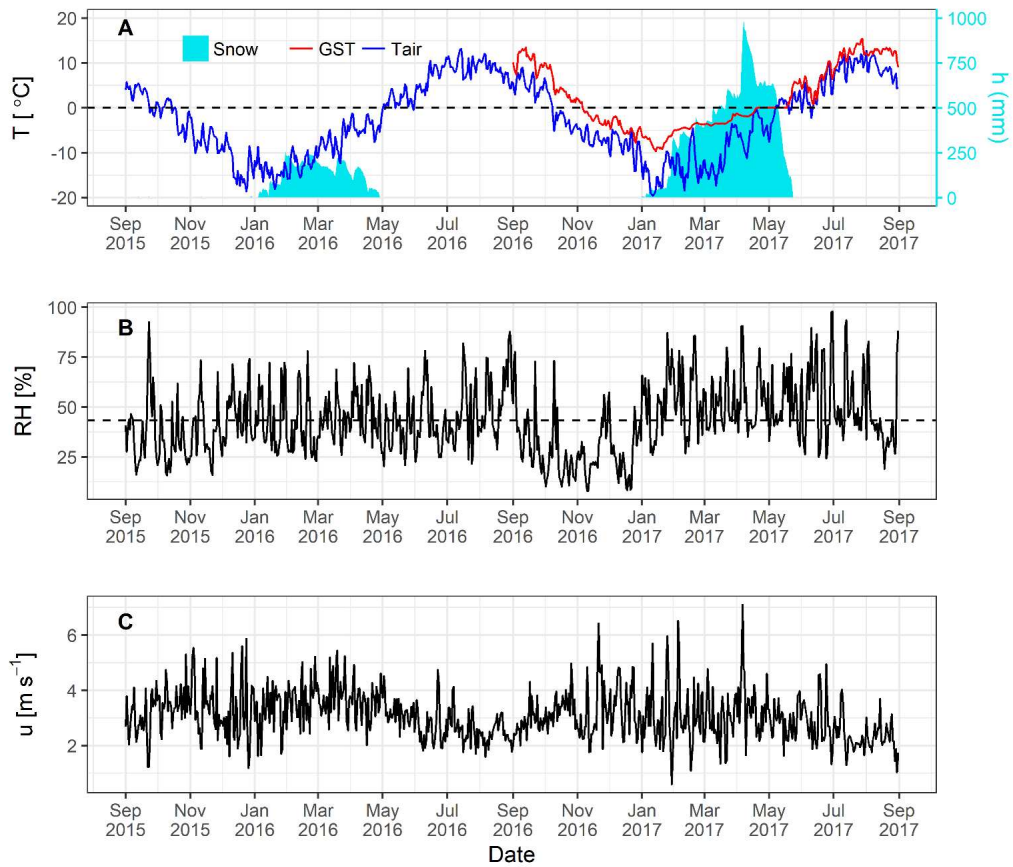
443 **4.2 Meteorological characteristics**

444 The range of the meteorological variables measured at [the](#) South-Pullu (4727 m a.s.l.) study
 445 site is given in Table 2 to provide an overview of the prevailing weather [conditions](#) in the study
 446 region. The daily mean air temperature (T_a) throughout the study period varies between -19.5
 447 to 13.1 °C with a mean annual average temperature (MAAT) of -2.5 °C (Figure 5A). [The](#)- T_a
 448 shows significant seasonal variations and [instantaneous-measured](#) hourly temperatures at the
 449 study site range between -23.7 °C in January and 18.1 °C in July. During the two-year study
 450 period, sub-zero mean monthly temperature prevailed for seven months from October to April
 451 in both [the](#) years [\(2015-16 and 2016-17\)](#). The monthly mean T_a during pre-winter months
 452 (September to December) of 2015-16 and 2016-17 was -4.6 and -2.7 °C, respectively. During
 453 the core winter months (January to February) of 2015-16 and 2016-17, the respective monthly
 454 mean T_a was -13.1 and -13.7 °C, [for](#) [C.](#) [for](#) post-winter months (March and April), mean

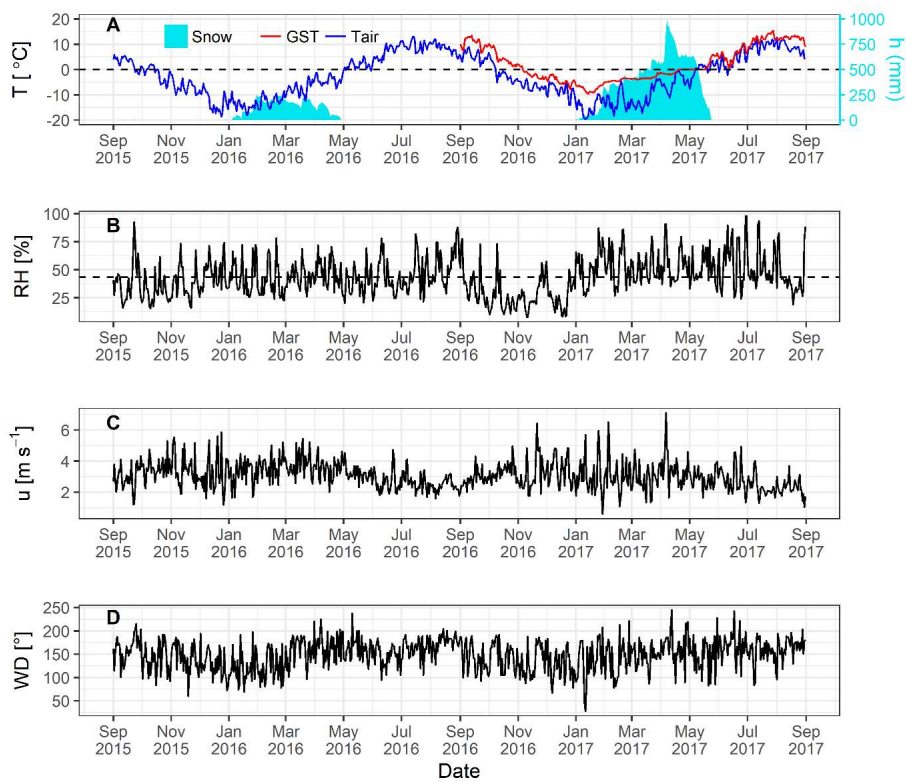
455 monthly T_a was -5.8 and -8 °C, respectively. For summer months (May to August), the
456 respective monthly mean T_a was 6.6 and 5.5 °C. A sudden change in the mean monthly T_a
457 characterises the onset of a new season, and the most evident inter-season change was found
458 between the winter and summer with a difference of about 16 °C ~~during-for~~ both ~~the~~ years.

459 The mean daily GST recorded by the logger near the AWS ~~available for one year~~ (1 September
460 2016 to 31 August 2017) is ~~also~~ plotted along with air temperature (Figure 5A). The mean daily
461 GST ranges from -9.7 to 15.4 °C with ~~a~~ mean annual GST of 2.1 °C. ~~The instantaneous hourly~~
462 ~~GST at the study site range between -10.7 °C in December and 20.2 °C in July.~~ The GST
463 followed the pattern of air temperature; but ~~damped~~ during winter ~~due to the insulating effect~~
464 ~~of~~; the snow cover ~~dampened the pattern.~~ The GST was ~~generally~~ higher than ~~the~~ T_a except for
465 a short period during snowmelt. The snow depth shown in Figure 5A is ~~further~~ described in
466 sub-section 4.3.

467 Mean relative humidity (RH) was equal to 43% during the study period (Figure 5B). The daily
468 average wind speed (u) ranges between 0.6 (29 January 2017) to 7.1 m s⁻¹ (6 April 2017) with
469 a mean wind speed of 3.1 m s⁻¹ (Figure 5C). The instantaneous hourly u was plotted as a
470 function of wind direction (WD) (Figure S5) for the study period ~~and which showed that there~~
471 ~~is~~ a persistent dominance of katabatic and anabatic winds at the study site, which is typical of
472 a mountain environment. The ~~daily~~ average WD during the study period was southeast (148°)
473 ~~(Figure 5D).~~



474



475

476 Figure 5 Daily mean values of observed (A) air temperature (blue) and one-year GST (red) (T,
 477 °C), snow depth (mm) on the secondary axis; (B) relative humidity (RH, %) with a dashed line
 478 as mean RH; and (C) wind speed (u, ms^{-1}); and (D) wind direction (WD, °); at South-Pullu
 479 (4727 m a.s.l.) in the upper Ganglass catchment, Leh from 1 September 2015 to 31 August
 480 2017.

481 The daily measured [annual](#) total precipitation at the study site equals 97.8 and 153.4 mm w.e.
 482 during the years 2015–16 and 2016–17, respectively. After adding 23% under catch (Thayyen
 483 et al., 2015) [unpublished work] to the total snow measurements, the total precipitation amount
 484 equals ~~to~~ 120.3 and 190.6 mm w.e. for the years 2015–16 and 2016–17, respectively. During
 485 the study period, the observed highest single-day precipitation was 20 mm w.e. recorded on 23

Formatted: Highlight

486 September 2015, and the total number of precipitation days were limited to 63. The
487 snowfall occurs mostly during the winter period (December to March), with some years
488 witnessing extended intermittent snowfall till mid-June, as experienced in this study during the
489 year 2016-17.

490 The precipitation estimated by the ESOLIP approach at the study site equals 92.2 and 292.5
491 mm w.e. during the years 2015–16 and 2016–17, respectively. The comparison between
492 observed precipitation (mm w.e.) and the one estimated by the ESOLIP approach is given in
493 (Table SI). In Table SI, the difference between the observed precipitation (mm w.e.) and the
494 one estimated by the ESOLIP approach is mainly due to the under-catch of winter snow
495 recorded by the Ordinary Rain Gauge.

496 4.3 Observed radiation components and snow depth

497 The observed daily mean variability of different components of radiation, albedo and snow
498 depth from 1 September 2015 to 31 August 2017 at South-Pullu (4727 m a.s.l.) is shown in
499 Figure 6. Daily mean SW_{in} varies between 24 and 378 $W m^{-2}$ (Table 2). Highest hourly
500 instantaneous short wave radiation recorded during the study period was 1358 $W m^{-2}$. Such
501 high values of SW_{in} are typical of a high elevation arid-catchment (e.g., MacDonell et al.,
502 2013). Persistent snow cover during the peak winter period for both the years extending from
503 January to March, resulted in a strong reflection of SW_{in} radiation (Figure 6A). During most of
504 the non-snow period, mean daily SW_{out} radiation (Figure 6A) remain more or less stable below
505 $100 W m^{-2}$. Daily mean SW_{out} varies between 2.4 and 262.6 $W m^{-2}$ with a mean value of 83.3
506 $W m^{-2}$ (Table 2). The daily mean LW_{in} shows high variations and ranges between 109 and 345
507 $W m^{-2}$ with an average of 220 $W m^{-2}$ (Figure 3B, Table 2), whereas LW_{out} was relatively
508 stable and varied between 211 and 400 $W m^{-2}$ with an average of 308 $W m^{-2}$ (Figure 6B, Table
509 2). The LW_{out} shows higher daily fluctuations during the summer months as compared to the
510 core winter months. The daily mean SW_{in} during the study period ranges between 2.5 and 319

Formatted: Space After: 8 pt

511 ~~W m⁻² with a mean value of 127 W m⁻². The~~ SW_n follows the pattern of SW_{in}, and for both the
512 years, during the wintertime, the SW_n was close to zero due to the high reflectivity of snow
513 (Figure 3C). ~~The daily mean LW_n varies between -163 and 17 W m⁻². The LW_n values~~ does
514 not show any seasonality and remain more or less constant with a mean value of -88 W m⁻²
515 (Figure 6C).

516 ~~The~~ mean daily observed R_n values ranges from -80.5 to 227.1 W m⁻² with a mean value of
517 39.4 W m⁻² (Table 2). During both ~~the~~ years, 2015–16 and 2016–17, the R_n was high in summer
518 and autumn but low in winter and spring. From January to early April (2015–16) and January
519 to early May (2016–17), when the surface was covered with seasonal snow, the R_n rapidly
520 declined to low values, or even became negative (Figure 6D). ~~Albedo (α) is calculated as the~~
521 ~~ratio of daily mean SW_{out} to daily mean SW_{in}. The α is of particular importance in the SEB and~~
522 ~~in the Earth's radiation balance that dictates the rate of heating of the land surface under~~
523 ~~different environmental conditions (Strugnell and Lucht, 2001). The~~ daily mean observed
524 albedo (α) at the study site ranges from 0.04 to 0.95, with a daily mean value of 0.43 (Figure
525 6E, Table 2). However, the value of broadband albedo is not greater than 0.85 (Roesch et al.,
526 2002), and the maximum value (0.95) recorded at the study site might be due to the instrumental
527 error. ~~The daily mean α was low in summer and high in winter and increased significantly~~
528 ~~when the ground surface was covered with snow (Figure 6E).~~

529 Both ~~the~~ years (2015–16 and 2016–17) experienced contrasting snow cover characteristics
530 during the study period (Figure 6F). The year 2015-16 experienced ~~shallow snow as heights~~
531 compared to 2016-17. During ~~the~~ 2015-16 year, the snowpack had a maximum depth of 258
532 mm on 30 January 2016, ~~whereas, during the 2016–17 year, the maximum was compared to~~ 991
533 mm on 07 April 2017. ~~The~~ snow cover duration was 120 days during ~~low snow year~~ (2015-
534 16) and 142 days during ~~the high snow year~~ (2016–17). The site became snow-free on 27 April
535 in 2016 and on 23 May in 2017. Higher elevations of the catchment become snow-free around

536 15 July in 2016 while the snow cover at glacier elevations persisted till 22 August in 2017. For
 537 ~~In both the year's, the~~ snow cover at lower elevations ~~initiated-started to build up~~ by the end
 538 of December, ~~and-while~~ the catchment experienced sub-zero mean monthly temperatures
 539 ~~already~~ since October.

540

541

542

543

544

545

546

547

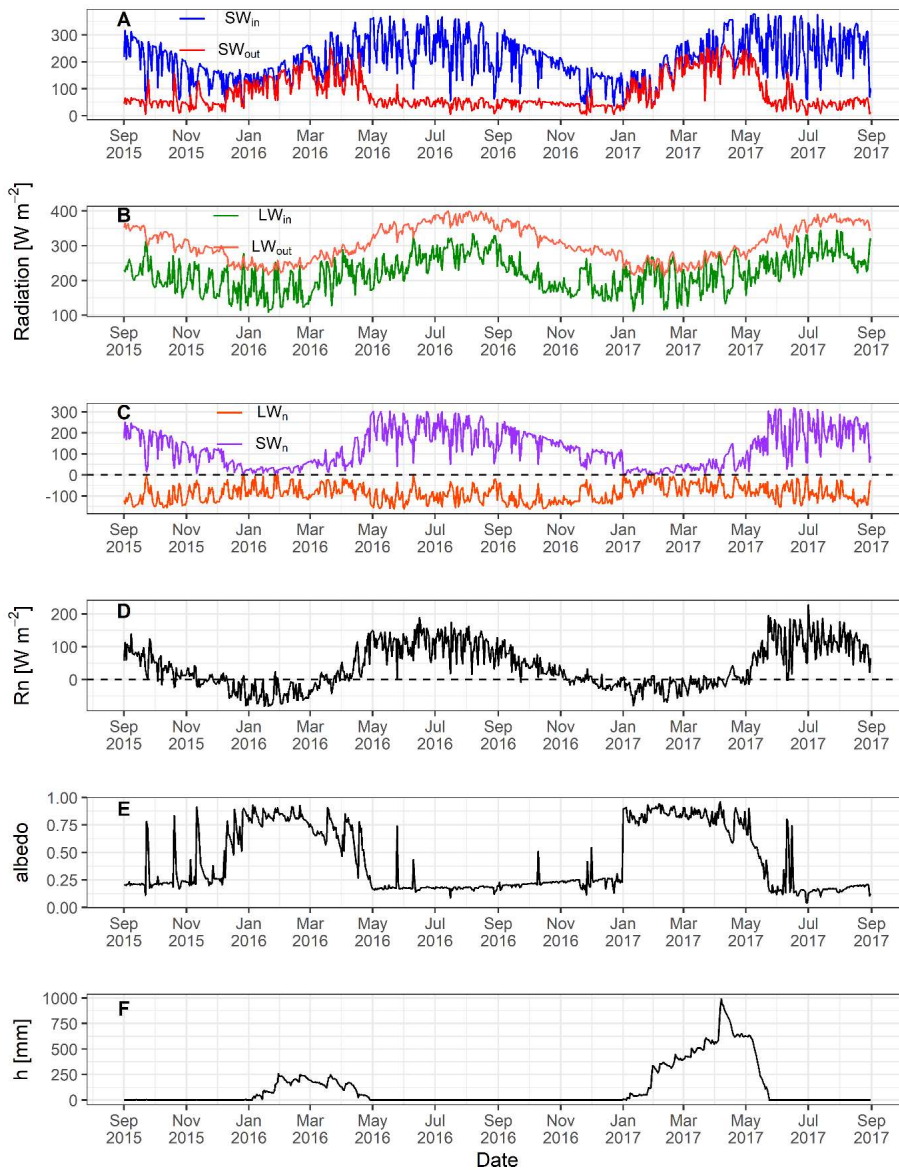
548 Table 2 ~~Two year +R~~ange of observed daily mean radiation components (SW_{in} , SW_{out} , LW_{in}
 549 and LW_{out} , SW_n , LW_n), surface albedo (α), net shortwave and longwave radiation (SW_n and
 550 LW_n), air temperature (T_a), wind speed (u), relative humidity (RH), precipitation (P), and snow
 551 depth (h) for the study period (1 September 2015 to 31 August 2017) at South-Pullu (4727 m
 552 a.s.l.).

Formatted: Normal, Line spacing: single

Variable	Units	Min.	Max.	Mean
SW_{in}	$W m^{-2}$	24.1	377.8	210.4
SW_{out}	$W m^{-2}$	(-)2.4	(-)262.6	(-)83.4
α	-	0.04	0.95	0.43
LW_{in}	$W m^{-2}$	109.0	344.7	220.4
LW_{out}	$W m^{-2}$	(-)211.3	(-)400.0	(-)308.0
SW_n	$W m^{-2}$	2.5	318.7	127.0
LW_n	$W m^{-2}$	-163	17.1	-87.6
T_a	$^{\circ}C$	-19.5	13.1	-2.5

u	m s^{-1}	0.6	7.1	3.1
RH	%	8	98	43.3
P	mm w.e	0	24.6	3
h	mm	0	991	-

553



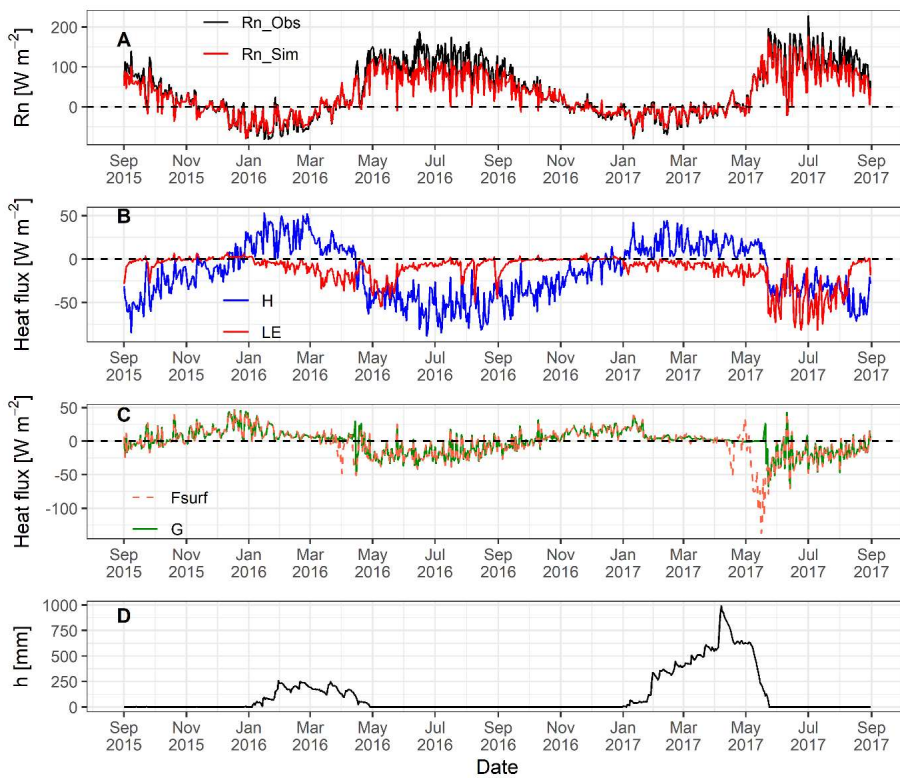
554

555 Figure 6 Observed daily mean values of (A) incoming (SW_{in}) and outgoing (SW_{out}) shortwave
556 radiation, (B) incoming (LW_{in}) and outgoing longwave (LW_{out}) radiation, (C) net shortwave
557 (SW_n) and longwave radiation (LW_n), and (D) net radiation (R_n), (E) surface albedo and (F)
558 snow depth (h, mm) at South-Pullu (4727 m a.s.l.) from 1 September 2015 to 31 August 2017.

559 4.4 Modelled surface energy balance

560 The mean daily variability of ~~modelled surface energy balance (SEB)~~ components is shown in
561 Figure 7. ~~The average Simulated mean~~ daily ~~simulated~~ R_n ~~values~~ ranges between -78.9 to 175.6
562 $W m^{-2}$ with a mean value of 29.7 $W m^{-2}$. ~~The~~ R_n shows the seasonal variability and decreases
563 as the ground surface gets covered by seasonal snow cover during wintertime, and increases as
564 the ground surface become snow-free (Figure 7A). ~~From December to March of both the years~~
565 ~~(2015-16 and 2016-17), R_n decreases and is negative during snow accumulation and remains~~
566 ~~close to zero during the melting time. For the rest of the time, R_n remains positive.~~ The
567 simulated R_n matches the observed R_n (Figure 7A), which shows that the LW_{out} was estimated
568 very well by the model. The daily mean sensible heat flux (H) ranges between -88.6 to 53 W
569 m^{-2} with a mean value of -15.6 $W m^{-2}$. ~~The~~ H is positive from January to April (2015-16) and
570 January to June (2016-17) due to the presence of seasonal snow cover (Figure 7B). During the
571 Rest of the period, H remains negative and larger ($\sim 35 W m^{-2}$) for most of the time. The
572 seasonal variation in H points to a ~~broader-larger~~ temperature gradient in summer than in
573 winter. The daily mean latent heat flux (LE) ranges between -81.4 to 7.6 $W m^{-2}$ with a mean
574 value of -11.2 $W m^{-2}$. During the snow-free freezing period (October to December) ~~of in~~ both
575 ~~the~~ years, ~~the~~ LE increases (from negative to zero) due to the freezing of soil moisture ~~content~~
576 ~~in the soil~~ and ~~also~~ fluctuates close to zero. ~~Furthermore, When the~~ surface is covered
577 by seasonal snow is on the ground, the LE is negative, ~~indicating~~ sublimation, and keeps
578 increasing (more negative) after snowmelt indicating evaporation ~~is taking place~~.

579 The heat conduction into the ground G is remains relatively a comparatively smaller component
 580 in the SEB (Figure 7C). The mean daily G values ranges between -70.9 to 46.3 W m^{-2} with
 581 a mean value of -0.5 W m^{-2} . The sign of the G , which shifted from negative during summer to
 582 positive during winter, is a function of the annual energy cycle. The heat flux available at the
 583 surface for melting (F_{surf}) ranges between -137 to 46.3 W m^{-2} with a mean value of -2.8 W m^{-2}
 584 (Table 3). During the summer, when snow-melting conditions were prevailing, the F_{surf} turns
 585 negative as a result of energy available for melt (Figure 7C). The positive F_{surf} during
 586 summertime (when melting conditions are prevailing at the surface) is the energy used to
 587 refreeze the meltwater and represents the freezing heat flux.



588

589 |Figure 7 GEOtop simulated daily mean values of surface energy balance components (A)
590 |observed and simulated net radiation (R_n), (B) sensible (H) and latent (LE) heat flux, (C)
591 |ground heat flux (G) and surface heat flux (F_{surf}) and (D) snow depth (h) at South-Pullu (4727
592 |m a.s.l.) from 1 September 2015 to 31 August 2017.

593
594
595
596
597
598
599

Formatted: Normal, Justified, Keep with next

600 | Table 3 Mean daily range of GEOtop simulated SEB ($W\ m^{-2}$) components for the study period
601 |(1 September 2015 to 31 August 2017) at South-Pullu (4727 m a.s.l.).

Variable	Min.	Max.	Mean
R_n	-78.9	175.6	29.7
H	-88.6	53.0	-15.6
LE	-81.4	7.6	-11.2
G	-70.9	46.3	-0.5
F_{surf}	-137.0	46.3	-2.8

602

603 | The ~~average~~-seasonal ~~response of~~ diurnal variation of modelled SEB components (R_n , LE, H
604 | and G) for ~~the 2015–16 and 2016–17~~both years are shown in ~~Supplementary~~-Figures S6 and
605 | S7, respectively ~~and is described in detail in the supplementary material.~~ ~~The~~ ~~The seasons~~

Formatted: Not Highlight

Formatted: Not Highlight

606 chosen were pre-winter (Sep to Dec), winter (Jan to Apr), post-winter (May-Jun), and summer
607 (Jul to Aug).

608 In the 2015–16 year (Figure S6), the amplitude of R_n and the G during pre-winter, post-winter
609 and summer season were the largest and smallest in winter. The G peaks earlier than those of
610 the LE and H during the pre-winter, post-winter and summer season. The LE and H show strong
611 seasonal characteristics such as (a) during the pre-winter season, the magnitude of diurnal
612 variation of H was greater than LE depicting lesser soil moisture content because of freezing
613 conditions at that time, (b) during the winter season, the amplitude of LE was slightly greater
614 (sublimation process) than H, (c) during the post-winter, the amplitude of H was greater than
615 LE and, (d) during the summer season, again the amplitude of H was greater than LE, which is
616 similar to that of the pattern seen during the pre-winter season. In the 2015–16 year, the
617 amplitude of LE in comparison to H was smaller in summer season due to the lesser
618 precipitation and lesser moisture availability. The R_n and G increased rapidly after the sunrise
619 and changed the direction during pre-winter, post-winter and summer seasons. After sunset,
620 the R_n and G again change sign rapidly, but the LE and H gradually decreased to lower values.
621 The LE and H in the morning increased 1 to 2 hours after the R_n during pre-, post-winter and
622 summer season.

623 In the 2016–17 year (Figure S7), the pre-winter, winter and summer were the same as that of
624 the 2015–16 year except for the amplitude of LE in was larger in summer season due to the
625 more precipitation and more moisture availability. However, during the winter and post-winter
626 season of the 2016–17 year, the main difference in diurnal changes was found during the winter
627 and post-winter season of 2016–17 because of the extended snow cover till May during that
628 year and is discussed in detail in sub-section 5.1. The amplitude of R_n , LE, H and G were smaller
629 compared to the 2015–16 year.

Formatted: Space After: 8 pt

630 During the study period, the proportional contribution of all SEB components shows that the
631 net radiation component dominates (80%), ~~the SEB~~ followed by H (9%) and LE fluxes (5%).
632 The ground heat flux (G) ~~G~~ was limited to 5% of the total flux, and 1% was used for melting
633 the seasonal snow. The proportional contribution of each flux percentages of the energy fluxes
634 was calculated by following the approach of Zhang et al. (2013). The mean monthly modelled
635 SEB components for both ~~the~~ years are given in Table S2.

636 Furthermore, during the study period, the partitioning of the energy balance shows that 52% (-
637 15.6 W m⁻²) of R_n (29.7 W m⁻²) was converted into H, 38% (-11.2 W m⁻²) into LE, 1% (-0.5 W
638 m⁻²) into G and 9% (-2.8 W m⁻²) for melting of seasonal snow. The partitioning was calculated
639 by taking the mean annual average of each of the individual SEB components (LE, H and G)
640 and then divide these respective averages with the mean annual average of R_n. However, a
641 distinct variation of energy flux is observed during the months of May-June of 2016-17 due to
642 the long-lasting snow cover, when one of the years (2016-17) experienced extended snow.

643 4.5 Comparison of seasonal distinction-variation of SEB during low and high snow 644 years

645 ~~A~~ The seasonal distinction-variation of observed radiation (SW_{in}, LW_{in}, SW_{out}, LW_{out}, SW_n,
646 LW_n,) and modelled SEB components -(R_n, LE, H, G and F_{surf}) for the low and high snow years
647 of the study period is analysed (Table 4). In addition to winter and summer, The seasons were
648 defined as winter (Sep-April) and summer (May-Aug) (Table 4). ~~T~~ these seasons were further
649 divided into two sub-seasons, each such as i.e. early winter (Sep, Oct, Nov and Dec) and peak
650 winter with snow (Jan, Feb, Mar and Apr). Similarly, the summer season was divided into ~~two~~
651 sub seasons called early summer (May and June; some years with extended snow) and peak
652 summer (July and August).

653

Formatted: Normal, Justified, Line spacing: Double

654 Table 4: Mean seasonal values of observed radiation and modelled surface energy balance
 655 components.

SEB Components [W m ⁻²]	2015-16				2016-17			
	Winter (Sep to Apr)		Summer (May to Aug)		Winter (Sep to Apr)		Summer (May to Aug)	
	Sep to Dec (Non-Snow)	Jan to Apr (Snow)	May to Jun (Non-Snow)	Jul-Aug (Peak Summer)	Sep to Dec (Non-Snow)	Jan to Apr (Snow)	May to Jun (Extended Snow)	Jul-Aug (Peak Summer)
SW _{in}	177.7	196.0	271.3	245.8	179.2	192.1	262.9	253.7
LW _{in}	203.0	190.5	244.5	286.5	198.0	202.5	245.9	277.0
SW _{out}	57.5	135.4	49.9	44.3	41.0	156.4	86.7	43.7
LW _{out}	310.3	259.5	379.1	412.4	317.9	251.9	337.9	399.3
SW _n	120.2	60.5	221.4	201.5	138.3	35.7	176.2	210.0
LW _n	-107.2	-69.0	-134.5	-125.9	-119.9	-49.4	-92.0	-122.3
R _n	12.9	-8.5	86.9	75.6	18.4	-13.7	84.2	87.7
LE	-1.2	-11.5	-18.9	-7.5	-1.1	-7.7	-33.1	-31.5
H	-21.7	15.7	-47.6	-54.0	-24.3	16.1	-15.9	-40.0
G	10.0	6.8	-20.3	-14.1	7.0	6.2	-14.6	-16.3
F _{surf}	0.1	2.5	0.0	0.1	0.0	0.9	20.6	0.0

656

657 ~~The mean seasonal variability of energy fluxes during these four major seasons is shown in~~
 658 ~~Table 4.~~ The mean seasonal SW_{in} ~~was comparable in~~ ~~were comparable for~~ all the seasons,
 659 whereas SW_{out} ~~was~~ significantly higher (86.7 W m⁻²) during ~~the~~ early summer season of 2016-
 660 17 ~~period on account of~~ ~~due to the~~ extended snow cover ~~as~~ compared to the preceding low
 661 snow year (49.9 W m⁻²). Similarly, LW_{in} shows ~~comparable similar~~ seasonal values during the
 662 observation period, ~~and whereas~~ LW_{out} ~~shows~~ a major difference during the early summer
 663 season with extended snow in 2016-17 ~~reducing with reduced~~ LW_{out} ~~-(337.9 W m⁻²) as~~
 664 compared to ~~the~~ corresponding period in 2015-16 (379.1 W m⁻²).

665 ~~In both the years,~~ ~~observed~~ comparable SW_n ~~values~~ during the early winter period ~~were~~
 666 ~~observed~~. However, during the peak snow season of ~~the 2016-17 year,~~ ~~the~~ SW_n was
 667 ~~comparatively~~ smaller (35.7 W m⁻²) ~~as~~ compared to 2015-16 (60.5 W m⁻²). Similarly,
 668 comparable SW_n during the peak summer season of both ~~the~~ years is contrasted by lower SW_n
 669 (176.2 W m⁻²) ~~in the of~~ early summer period of 2017 as compared to 221.4 W m⁻² in 2016, on
 670 account of extended snow cover. The same trend is ~~seen~~ ~~reordered~~ for LW_n as well, with a lower

671 value ~~during the extended snow~~ (-92 W m^{-2}) in 2017 as compared to 2016 (-134.5 W m^{-2}).
672 Seasonal variations in R_n followed the pattern of SW_n . ~~Both the year's observed comparable R_n~~
673 ~~during the early snow-free winter period. However, the R_n was comparatively lower (-13.7 W~~
674 ~~m^{-2}) during the peak snow season of 2016-17 as compared to 2015-16 (-8.5 W m^{-2}).~~
675 ~~However, The~~ most significant difference of R_n is observed during early summer (May-June)
676 and peak summer (Jul-Aug) of 2016 and 2017, respectively.

677 ~~In b~~Both the years, ~~a~~ observed comparable LE flux during the winter season ~~is observed~~. A
678 key difference ~~is seen during in LE flux is observed during extended snow and peak summer~~
679 ~~sub-season of 2016 and 2017. In~~ the peak summer sub-season of 2016-17, ~~the where~~ LE was
680 higher (-31.5 W m^{-2}) as compared to the 2015-16 (-7.5 W m^{-2}). The reason behind this is due
681 to the ~~lesser amount of reduced~~ soil water content availability for evaporation during 2015-16
682 in comparison to ~~the~~ high snow year 2016-17. The comparatively large ~~er~~ LE ~~values~~ during the
683 snow sub-season ~~of in~~ both ~~the~~ years shows that sublimation is a -key factor in the region. The
684 ~~H-H~~ flux was ~~comparable similar~~ during the winter season ~~of in~~ both ~~the~~ years. ~~During the peak~~
685 ~~summer sub-season of the 2015-16 year, the H was slightly larger (-54 W m^{-2}) as compared to~~
686 ~~2016-17 (-40 W m^{-2}).~~ The critical difference in H ~~flux~~ was observed during the extended snow
687 sub-season of ~~the~~ 2016-17 ~~year~~ when H was much smaller (-15.9 W m^{-2}) compared to 2015-
688 16 (-47.6 W m^{-2}) owing to the extended snow cover ~~in during the 2016-17 year~~.

689 ~~During the winter season of both the years, the G was positive and changed the sign to negative~~
690 ~~during the summer season. Overall, G is comparatively a smaller component. The m~~Mean
691 seasonal F_{surf} ~~values were~~ was almost equal to zero during all ~~the~~ seasons except during the
692 snow sub-season of both ~~the~~ years and extended snow sub-season of ~~the~~ 2016-17 ~~year~~,
693 ~~where~~ The F_{surf} (heat flux available for melt) was much higher (20.6 W m^{-2}) ~~than during 2015-~~
694 ~~16 during the extended snow sub-season of the 2016-17 year~~. From this ~~e~~ inter-year seasonal

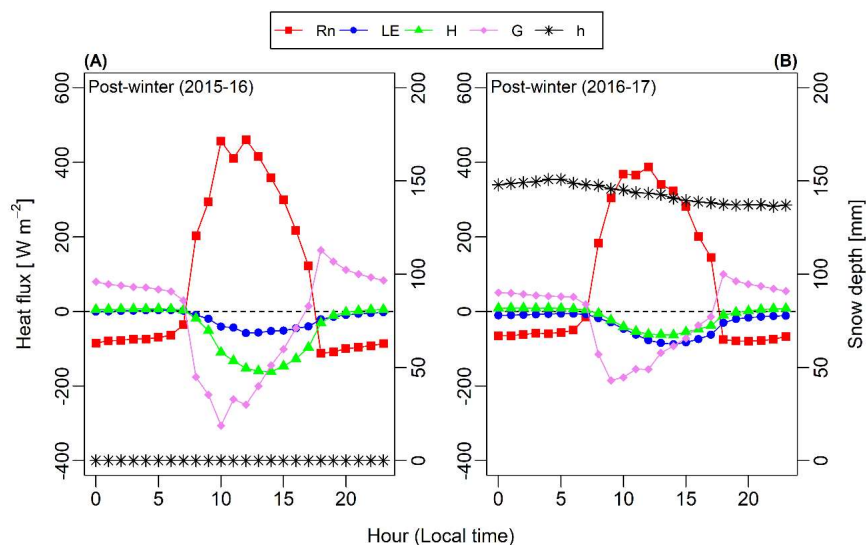
695 comparison, it was found that the extended snow sub-season of ~~the~~ 2016-17 (high snow year)
696 forced significant differences in energy fluxes between the years.

697 **5 Discussion**

698 **5.1 ~~A distinction of~~ SEB variations during low and high snow years**

699 Realistic reproduction of seasonal and inter-annual variations in snow depth during the low
700 (2015–16) and high snow (2016–17) years ~~points towards the~~indicate a credible simulation of
701 the SEB during the study period. We further investigated the response of SEB components
702 during these years with contrasting snow cover for a better understanding of the critical periods
703 of meteorological forcing and its characteristics.

704 ~~To analyse this in more detail~~understand the critical periods of meteorological forcing and its
705 effect on modelled SEB fluxes, we will discuss the diurnal variation of modelled SEB during
706 the critical season~~only for one season~~, i.e., early summer ~~season~~, which showed ~~significant~~
707 differences in the amplitude of the energy fluxes (Figure 8). During ~~the~~ early winter, peak
708 winter and peak summer seasons (Figure *S6, S7*), the diurnal variations of the SEB fluxes for
709 the 2015-16 year were more or less similar in comparison to the 2016-17 year. However, during
710 the early summer season of both ~~the~~ years (Figure 8), the SEB fluxes show different diurnal
711 characteristics. ~~In~~ During early summer season of the 2016–17 year, the main difference in
712 diurnal changes was found because of the extended snow cover till May during that year. For
713 ~~the~~ 2016–17 year, the diurnal amplitude of R_n was slightly larger, whereas, all other
714 components (LE, H and G) were of almost zero amplitude (Figure 8B). The smaller amplitude
715 of LE, H and G is due to the smaller input (solar radiation) and the extended seasonal snow on
716 the ground. ~~Therefore, we can say that the different SEB characteristics during these two years~~
717 is in response to the forcing of precipitation via snowfall.



719

720 Figure 8 The diurnal change of GEOTop modelled seasonal surface energy fluxes for (A) early
 721 summer 2015-16, and (B) early summer 2016-17 at South-Pullu (4727 m a.s.l.), in the upper
 722 Ganglass catchment, Leh. The seasonal snow depth is plotted on the secondary axis.

723 5.2 Impact of freezing and thawing process on surface energy fluxes

724 To understand the impact of freeze/thaw processes on surface energy fluxes, the variability of
 725 SEB components is [discussed here \(shown in Figure 9\)](#). The aim is to [make-highlight](#) the
 726 [measurements of the study site as an exemplar-example-of-for](#) SEB processes [for-the-over](#)
 727 seasonal frozen ground and permafrost in the cold-arid Indian Himalayan Region.

728 [Comparatively, the \$R_n\$ was higher at the study site due to the higher elevation, aridity and sparse](#)
 729 [vegetation.](#)

Formatted: Highlight

730 The freeze and thaw processes in the ground are complex and involve several physical and
 731 chemical changes, which include energy exchange, phase change, etc. (Chen et al., 2014; Hu
 732 et al., 2019). These processes amplify the interaction of fluxes between soil and atmosphere
 733 (Chen et al., 2014). [In addition to the effect of seasonal snow, the \$R_n\$ can also get affected by](#)

Formatted: Not Highlight

734 [the seasonal freeze-thaw process of the ground. For example, when the seasonal frozen](#)
735 [ground/permafrost begins to thaw in summer, \$R_n\$ \(Figure 9A\) increases due to the lower albedo](#)
736 [of water than ice \(Yao et al., 2020\), and the opposite pattern happens during the freezing season.](#)

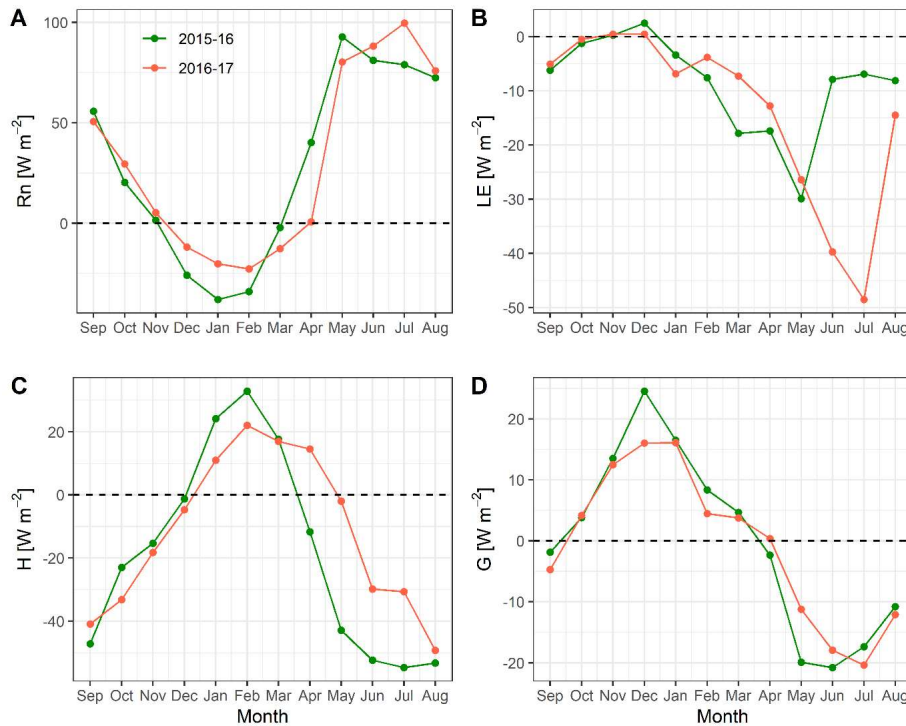
Formatted: Subscript

737 In Figure 9D, during the seasonal freezing phase from September to December, the simulated
738 mean monthly G starts to decrease and begins to change the sign from negative to positive due
739 to the ~~transfer change~~ of flux [direction](#) from soil to the atmosphere. However, during summers,
740 the permafrost and ~~the~~ seasonally frozen soil act as a heat sink, because the thawing processes
741 require a considerable amount of heat that is absorbed from the atmosphere ~~to~~ [by](#) the soil
742 (Eugster et al., 2000; Gu et al., 2015). In Figure 9D, during the thawing phase from April to
743 July, the simulated mean monthly G starts to increase and changes sign due to the transfer of
744 flux [direction](#) from the atmosphere to the soil. This pattern is consistent with the [results from](#)
745 [other](#) studies on permafrost areas from the Tibetan Plateau (Chen et al., 2014; Hu et al., 2019;
746 Zhao et al., 2000). In both low and high snow years (Figure 9B and 9C), the mean monthly
747 estimated H and LE heat fluxes show prominent seasonal characteristics, such as the latent heat
748 flux was highest in summer and lowest in winter. In contrast, the sensible heat flux was highest
749 in early summer and gradually decreased towards the pre-winter season. ~~Similar~~ [A similar](#) kind
750 of variability in the LE and H is also reported from the seasonally frozen ground and permafrost
751 regions of the Tibetan plateau (Gu et al., 2015; Yao et al., 2011, 2020).

752 ~~Furthermore, in Figure 9C, d~~ During the peak summer months (June to August, [Figure 9C](#)), ~~the~~
753 H tends to decrease or became relatively stable. This is [mostly-primarily](#) due to the thawing in
754 the seasonally frozen ground resulting in a sensible heat sink (Eugster et al., 2000).

755 ~~In~~ [On](#) the Tibetan Plateau, the main reasons for the seasonal variability of the turbulent fluxes
756 are due to the Asian monsoon and the freezing and thawing processes of the active layer (~~Yao~~
757 ~~et al., 2011~~); ([Yao et al., 2011](#)); however, ~~in~~ [at](#) our study site, the monsoon precipitation is not

758 a dominant factor. ~~Therefore, freeze~~Therefore, freeze/thaw processes are the key factor
 759 regulating the turbulent heat fluxes during summers.



760
 761 Figure 9: Comparison of estimated mean monthly surface energy balance components ($W m^{-2}$)
 762 ²) (A) R_n , (B) LE, (C) H, and (D) G for the low (2015-16) and high (2016-17) snow years, at
 763 South-Pullu (4727 m a.s.l.).

764 **5.3 Comparison with other environments**

765 In this section, the observed radiation and estimated SEB components from our cold-arid
 766 catchment in Ladakh, India, are compared with other cryospheric systems, globally (Table 5).

767 In addition to several Although aiming to represent differing permafrost environments around
 768 the world, this comparison also includes SEB studies on glaciers for lack of additional

769 ~~data~~comparison. In most of the studies referred here, the radiation components are measured,
770 and the turbulent (H and LE) and ground (G) heat fluxes are modelled.

771 Based on the comparison, the SW_{in} values at ~~the our~~ study site is comparable with ~~data from~~
772 ~~the~~ Tibetan plateau (Mölg et al., 2012; Zhang et al., 2013; Zhu et al., 2015) ~~and but~~ significantly
773 ~~much~~ higher than the values reported from other studies such as the ~~European Alps~~ (Oerlemans
774 and Klok, 2002; Stocker-Mittaz, 2002). ~~The Similarly,~~ LW_{in} values at ~~the our~~ study site ~~was~~
775 ~~are~~ comparable with values observed at ~~the~~ Tibetan Plateau (Zhang et al., 2013; Zhu et al.,
776 2015) and smaller than ~~the reported from~~ other studies except for Antarctica. At ~~the our~~ study
777 site, the SW_n was the largest source of energy and LW_n the most considerable energy loss and
778 strongly negative, and both were higher than those reported in other studies (Table 5), ~~except~~
779 ~~for. However,~~ the Andes ~~were an exception~~ (Favier, 2004; Pellicciotti et al., 2008).

780 The different surface albedo (α) values help to distinguish the surface characteristics. ~~Not~~
781 ~~surprisingly,~~ ~~The~~ mean α for all ~~the bedrock or tundra vegetation~~ sites (Table 5) ~~where~~
782 ~~radiation balance is measured either on bedrock or tundra vegetation~~ was smaller than ~~for those~~
783 ~~measured oversites with~~ firn or ice ~~cover~~ during summer, with few exceptions. Albedo ~~ranges~~
784 ~~values~~ for glacier ice ~~range~~ from 0.5 to 0.7 and for tundra/bedrock from 0.25 to 0.54.
785 Comparison of RH for the study period shows that the mean measured RH (43 %) was much
786 smaller than ~~observed in~~ other regions except in the semi-arid Andes (Pellicciotti et al., 2008),
787 where the RH ~~values was are~~ comparable. Furthermore, the mean annual precipitation in
788 ~~our this~~ study was also lower than in the other areas compared.

789 Based on the comparison of measured radiation and meteorological variables with other, better-
790 investigated regions of the world (Table 5), it was observed that our study area is unique in
791 terms of ~~lower~~ RH (43% compared to ~70% in the ~~European Alps~~) and cloudiness, leading to
792 ~~(a) R~~reduced LW_{in} and strongly negative LW_n (~90 W m⁻² on average, ~~which is~~ much more
793 than in the ~~European Alps~~). Hence, the high elevation cold-arid region land surfaces could be

Formatted: Font: 12 pt

Formatted: Font: 12 pt

Formatted: Font: 12 pt

Formatted: Font: 12 pt

Formatted: Font: 12 pt

Formatted: Font: 12 pt

Formatted: Font: 12 pt

Field Code Changed

Formatted: Font: 12 pt

Formatted: Font: 12 pt

Formatted: Space After: 8 pt

794 overall colder than ~~the~~ locations with ~~more~~ higher RH. ~~(b)~~ In addition, an i increased SW_{in} leads
795 to larger radiation input on ~~;~~ ~~This will mean that~~ sun-exposed slopes will receive more radiation
796 and a reduction on shaded ~~ones less~~ slopes (less diffuse radiation) than in comparable areas.
797 Finally, an and (e) ~~I~~ increased cooling by stronger evaporation in wet places such as meadows
798 can be expected. Therefore, the warm sun-exposed dry areas and colder wet places could lead
799 to significant spatial inhomogeneity in permafrost distribution. ~~Further, it is apprehended that~~
800 ~~high incoming shortwave radiation over moist high elevation surfaces may be facilitating~~
801 ~~enhanced cooling of as a result of stronger evaporation.~~

802

803 Table 5: Comparison of mean annual observed radiation and estimated SEB components and
 804 meteorological variables with_for different regions of the world. (SW_{in} = Incoming shortwave
 805 radiation, SW_{out} = Outgoing shortwave radiation, albedo = α , LW_{in} = Incoming longwave
 806 radiation, LW_{out} = Outgoing longwave radiation, SW_n = Net shortwave radiation, LW_n = Net
 807 longwave radiation, RH = Relative humidity, R_n = Net radiation, LE = Latent heat flux, H =
 808 Sensible heat flux, G = Ground heat flux, SEB = energy available at surface, MAAT = Mean
 809 annual air temperature, P = Precipitation, NA = Not available). The-LE, H, and G are the
 810 modelled values. All the radiation components and heat fluxes are in units of $W\ m^{-2}$.

Formatted: Normal, Justified
 Formatted: Width: 8.27", Height: 11.69"

Variable	Leh	Tibetan Plateau	Swiss Alps		Tropical Andes	Semi-arid Andes	New Zealand (Alps)	Canada	Sub-Arctic	Greenland	High Arctic (Norway)				High Arctic
SW_{in}	210.4	230	136	149	239	344	140	136	101.3	110	79.5	122	78	108	124
SW_{out}	-83.4	-157	-72	-74	-116	-106	-93	-94	-25.7	-70	-39.5	-38	-42	-70	-79.7
α (-)	0.40	0.68	0.53	0.5	0.49	0.3	0.66	0.69	0.25	0.64	0.50	0.31	0.54	0.65	0.64
LW_{in}	220.4	221	NA	260	272	252	278	248	310	246	263.7	261	254	272	NA
LW_{out}	-308.0	-277	NA	-308	-311	306	-305	-278	-349.8	-281	-299.0	-300	-286	-292	NA
SW_n	127.0	73	64	75	123	238	48	42	75.6	40	40.0	84	36	38	44.3

Formatted: Indent: Left: 0.08", Right: 0.08"
 Formatted Table
 Formatted: Indent: Left: 0.08", Right: 0.08"
 Formatted: Indent: Left: 0.08", Right: 0.08"
 Formatted: Indent: Left: 0.08", Right: 0.08"
 Formatted: Indent: Left: 0.08", Right: 0.08"
 Formatted: Indent: Left: 0.08", Right: 0.08"

Surface type	Time period	P (mm)	MAAT (°C)	G	H	LE	R _n	RH (%)	LW _n
Bedrock/debris	Sep 2015 to Aug 2017	114	-2.5	-0.5	-15.6	-11.2	39.4	43.3	-87.6
Glacier ice	Aug 2010 to Jul 2012	1250	-6.3	2	13	-11	17	59	-56
Glacier ice	Jan to Dec 2000	NA	2.1	3	36	6	28	64	-36
Bedrock/debris	Feb 1997 to Jan 1998	NA	-1.1	-2	-3	-1	27	59	-48
Glacier ice	Mar 2002 to Mar 2003	970	0.3	NA	21	-27	84	81	-39
Glacier ice	11 Dec 2005-12 Feb 2006	NA	NA	3	56	-19	184	42	-54
Glacier ice	Oct 2010 to Sep 2012	NA	1.2	2	30	1	21	78	-27
Glacier ice	2002-2013	NA	-4.2	0.5	-5	-15	12	71	-30
Peatland	Jan to Dec 2013	369	6	1.9	2.9	NA	37.1	~75	-39.8
Glacier ice	Aug 2003 to Aug 2007	NA	-5.45	NA	NA	NA	4	75	-36
Tundra vegetation	Jan 2015 to Dec 2015	581.2	-2.86	NA	NA	NA	4.78	74.8	-35.3
Bedrock/debris	Jan to Dec 2000	800	-3.4	-3.5	-34.2	NA	45	83	-39
Tundra vegetation	Mar 2008 to Mar 2009	NA	-5.4	~0.5	-6.9	6.8	4	74	-32
Glacier ice	Sep 2001 to Sep 2006	NA	-1.9	3	15	1	18	77.9	-20
Ice sheet	Mar 2007 to Jan 2013	NA	-10.2	-0.12	28	-62.1	-4.9	50.8	-49.2
Ice sheet	Apr 1988 to Mar 1989	NA	-18	NA	1	NA	NA	NA	NA

Formatted: Indent: Left: 0.08", Right: 0.08"

Formatted: Indent: Left: 0.08", Right: 0.08"

Formatted: Indent: Left: 0.08", Right: 0.08"

Formatted: Indent: Left: 0.08", Right: 0.08"

Formatted: Indent: Left: 0.08", Right: 0.08"

Formatted: Indent: Left: 0.08", Right: 0.08"

Formatted: Indent: Left: 0.08", Right: 0.08"

Formatted: Indent: Left: 0.08", Right: 0.08"

Formatted: Indent: Left: 0.08", Right: 0.08"

Formatted: Indent: Left: 0.08", Right: 0.08"

Source	Latitude	Elevation (m)	Location
This Study	34.255° N	4727	Cold-arid, Ladakh
(Zhu et al., 2015)	30.476° N	5665	Zhadang Glacier, Tibetan Plateau
(Orlemans and Klok, 2002)	46.400° N	2100	Mortratschgletscher glacier.
(Stocker-Mittaz, 2002)	46.433° N	2700	Murtel-Corvatsch rock
(Favier, 2004)	0.467° S	4890	Antizana glacier 15, Ecuador
(Pellicciotti et al., 2008)	32.99056° S	3127	Juncal Norte Glacier, central Chile
(Cullen and Conway, 2015)	44.084° S	1760	Brewster Glacier, New Zealand
(Marshall, 2014)	50.717° N	2665	Haig Glacier, Canadian rocky
(Stiegler et al., 2016)	68.349° N	380	Peatland complex Stordalen,
(van den Broeke et al., 2008)	67.100° N	490	west Greenland ice sheet
(Boike et al., 2018)	78.551° N	25	Bayelva, Spitsbergen,
(Isaksen et al., 2003)	61.676° N	1894	Juvvasshøe, southern Norway
(Westermann et al., 2009)	78.917° N	25	Svalbard, Norway
(Giesen et al., 2009)	61.600° N	1570	Storbreen glacier, Norway
(Ganju and Gusain, 2017)	70.733° S	142	Schirmacher Oasis, Antarctica
(Bintanja et al., 1997)	74.48° S	115	Dronning Land, Antarctica

Formatted: Indent: Left: 0.08", Right: 0.08"

Formatted: Indent: Left: 0.08", Right: 0.08"

Formatted: Indent: Left: 0.08", Right: 0.08"

Formatted: Indent: Left: 0.08", Right: 0.08"

811

812 6 Conclusion

813 In the high-elevation, cold-arid regions of Ladakh, significant areas of permafrost occurrence
814 are highly likely (Wani et al., 2020), and large areas experience deep seasonal freeze-thaw. The
815 present study ~~is aimed at providing aims to provide the~~ first insight ~~on-into~~ the surface energy
816 balance characteristics of this permafrost environment.

817 For the period under study, the surface energy balance characteristics of the cold-arid site in
818 the Indian Himalayan region show that ~~the~~ net radiation was the major component with a mean
819 value of 29.7 W m⁻², followed by sensible heat flux (-15.6 W m⁻²) and latent heat flux (-11.2
820 W m⁻²), and the mean ground heat flux was equal to -0.5 W m⁻². During the study period, the

821 partitioning of surface energy balance shows that 52% of R_n was converted into H, 38% into
822 LE, 1% into G and 9% for melting of seasonal snow.

823 Among the two observation years, one was ~~characterised by a low-reduced snow cover~~
824 ~~compared to a much larger snow cover in the other year, year, and the another was high, and d~~
825 ~~During these low and high snow years, the energy utilised for melting-seasonal snow-melt~~ was
826 4% and 14% of R_n , respectively. During both ~~the~~-years, the latent heat flux was highest in
827 summer and lowest in winter, whereas the sensible heat flux was highest in post-winter and
828 gradually decreased towards the pre-winter season. For both low and high ~~snow~~ years, the
829 snowfall in the catchment occurred by the last week of December, facilitating the ground
830 cooling ~~by-during~~ almost three months (October to December) ~~of-with~~ sub-zero ~~air~~
831 temperatures up to -20 °C. The extended snow cover during the high snow year also insulates
832 the ground from ~~warmer-higher~~ temperature until May. Therefore, the late occurrence of snow
833 and extended snow cover could be the critical factors in controlling the thermal regime of
834 permafrost in the area.

835 A comparison of observed radiation and meteorological variables with other regions of the
836 world show that the study site/region at Ladakh ~~have-has~~ a very low relative humidity (RH) in
837 the range of 43% compared to, e.g. $\sim 70\%$ in the ~~European~~ Alps. Therefore, ~~the~~ rarefied and
838 dry atmosphere of the cold-arid Himalaya could be impacting the energy regime in multiple
839 ways: (a) ~~this results in the~~-reduced amount of incoming longwave radiation and strongly
840 negative net longwave radiation, (~~in the range of~~ -90 W m^{-2} compared to -40 W m^{-2} in the
841 ~~European~~ Alps) and therefore, leading to colder land surfaces as compared to ~~the~~-other
842 mountain environments with higher RH, (b) higher global shortwave radiation lead~~ings~~ to more
843 radiation received by sun-exposed slopes than shaded ones ~~in-comparable areas~~ and (c)
844 ~~increased cooling over~~ wet ~~areasplaces~~ such as meadows, etc. ~~experience-increased-cooling-as~~
845 a result of stronger evaporation. However, sun-exposed dry areas could be warmer, leading to

846 significant spatial inhomogeneity in permafrost distribution. The current study gives a first-
847 order overview of the surface energy balance from the cold-arid Himalaya in the context of
848 permafrost processes, and we hope this will encourage similar studies at other locations in the
849 region, which would significantly improve the understanding of the climate from the region.
850

851 **Acknowledgements**

852 John Mohd Wani acknowledges the Ministry of Human Resource Development (MHRD)
853 Government of India (GOI) fellowship for carrying out his PhD work. Renoj J. Thayyen thanks
854 the National Institute of Hydrology (NIH) Roorkee and SERB (Project No.
855 EMR/2015/000887) for funding the instrumentation in the Ganglass catchment. The first
856 insight into ~~the use of~~[fusing the](#) GEOTop permafrost spin up scheme by Joel Fiddes is highly
857 acknowledged. We acknowledge the developers of GEOTop, for keeping the software open-
858 source and free. The source code of the GEOTop model 2.0 (Endrizzi et al., 2014) used is freely
859 available at <https://github.com/geotopmodel/geotop/tree/sc27xx>. ~~The analysis of data~~[Data](#)
860 [analysis](#) was performed using R (R Core Team, 2016; Wickham, 2016, 2017; Wickham and
861 Francois, 2016; Wilke, 2019).

862 **Conflicts of interest**

863 The author(s) declare(s) that there is no conflict of interest.

864 **Author contributions**

865 JMW participated in data collection in the field, carried out the data analysis and processing,
866 run the GEOTop model and prepared the manuscript. RJT conceived the study, arranged field
867 instruments, organised fieldwork for instrumentation and data collection, contributed to the
868 data analysis and manuscript preparation. CSPO assisted in data analysis and manuscript
869 preparation. SG assisted in setting up GEOTop model, analysis of results and manuscript
870 preparation.

871 **References**

- 872 Ali, S. N., Quamar, M. F., Phartiyal, B. and Sharma, A.: Need for Permafrost Researches in
873 Indian Himalaya, *J. Clim. Chang.*, 4(1), 33–36, doi:10.3233/jcc-180004, 2018.
- 874 Allen, S. K., Fiddes, J., Linsbauer, A., Randhawa, S. S., Saklani, B. and Salzmann, N.:
875 Permafrost Studies in Kullu District, Himachal Pradesh, *Curr. Sci.*, 111(3), 550–553,
876 doi:10.18520/cs/v111/i3/550-553, 2016.
- 877 Azam, M. F., Wagnon, P., Vincent, C., Ramanathan, A. L., Favier, V., Mandal, A. and
878 Pottakkal, J. G.: Processes governing the mass balance of Chhota Shigri Glacier (western
879 Himalaya, India) assessed by point-scale surface energy balance measurements, *Cryosph.*,
880 8(6), 2195–2217, doi:10.5194/tc-8-2195-2014, 2014.
- 881 Baral, P., Haq, M. A. and Yaragal, S.: Assessment of rock glaciers and permafrost distribution
882 in Uttarakhand, India, *Permafr. Periglac. Process.*, (April 2018), 1–26, doi:10.1002/ppp.2008,
883 2019.
- 884 Bertoldi, G., Notarnicola, C., Leitinger, G., Endrizzi, S., Zebisch, M., Della Chiesa, S. and
885 Tappeiner, U.: Topographical and ecohydrological controls on land surface temperature in an
886 alpine catchment, *Ecohydrology*, 3(2), 189–204, doi:10.1002/eco.129, 2010.
- 887 Bhutiyani, M. R.: Mass-balance studies on Siachen Glacier in the Nubra valley, Karakoram
888 Himalaya, India, *J. Glaciol.*, 45(149), 112–118, doi:10.3189/S0022143000003099, 1999.
- 889 Bhutiyani, M. R., Kale, V. S. and Pawar, N. J.: Long-term trends in maximum, minimum and
890 mean annual air temperatures across the Northwestern Himalaya during the twentieth century,
891 *Clim. Change*, 85(1–2), 159–177, doi:10.1007/s10584-006-9196-1, 2007.
- 892 Bintanja, R., Jonsson, S. and Knap, W. H.: The annual cycle of the surface energy balance of
893 Antarctic blue ice, *J. Geophys. Res. Atmos.*, 102(D2), 1867–1881, doi:10.1029/96JD01801,
894 1997.
- 895 Boeckli, L., Brenning, A., Gruber, S. and Noetzli, J.: A statistical approach to modelling
896 permafrost distribution in the European Alps or similar mountain ranges, *Cryosph.*, 6(1), 125–

Formatted: Justified

897 140, doi:10.5194/tc-6-125-2012, 2012.

898 Boike, J., Wille, C. and Abnizova, A.: Climatology and summer energy and water balance of
899 polygonal tundra in the Lena River Delta, Siberia, *J. Geophys. Res.*, 113(G3), 1–15,
900 doi:10.1029/2007JG000540, 2008.

901 Boike, J., Juszak, I., Lange, S., Chadburn, S., Burke, E., Overduin, P. P., Roth, K., Ippisch, O.,
902 Bornemann, N., Stern, L., Gouttevin, I., Hauber, E. and Westermann, S.: A 20-year record
903 (1998-2017) of permafrost, active layer and meteorological conditions at a high Arctic
904 permafrost research site (Bayelva, Spitsbergen), *Earth Syst. Sci. Data*, 10(1), 355–390,
905 doi:10.5194/essd-10-355-2018, 2018.

906 Bolch, T., Kulkarni, A., Kääh, A., Huggel, C., Paul, F., Cogley, J. G., Frey, H., Kargel, J. S.,
907 Fujita, K., Scheel, M. and others: The state and fate of Himalayan glaciers, *Science* (80-.),
908 336(6079), 310–314, doi:10.1126/science.1215828, 2012.

909 Bolch, T., Shea, J. M., Liu, S., Azam, F. M., Gao, Y., Gruber, S., Immerzeel, W. W., Kulkarni,
910 A., Li, H., Tahir, A. A., Zhang, G. and Zhang, Y.: Status and Change of the Cryosphere in the
911 Extended Hindu Kush Himalaya Region, in *The Hindu Kush Himalaya Assessment*, edited by
912 P. Wester, A. Mishra, A. Mukherji, and A. B. Shrestha, pp. 209–255, Springer, Cham., 2019.

913 Bommer, C., Phillips, M. and Arenson, L. U.: Practical recommendations for planning,
914 constructing and maintaining infrastructure in mountain permafrost, *Permafr. Periglac.*
915 *Process.*, 21(1), 97–104, doi:10.1002/ppp.679, 2010.

916 van den Broeke, M., van As, D., Reijmer, C. and van de Wal, R.: Assessing and Improving the
917 Quality of Unattended Radiation Observations in Antarctica, *J. Atmos. Ocean. Technol.*, 21(9),
918 1417–1431, doi:10.1175/1520-0426(2004)021<1417:AAITQO>2.0.CO;2, 2004.

919 van den Broeke, M., Smeets, P., Ettema, J. and Munneke, P. K.: Surface radiation balance in
920 the ablation zone of the west Greenland ice sheet, *J. Geophys. Res.*, 113(D13), 1–14,
921 doi:10.1029/2007JD009283, 2008.

922 Brutsaert, W.: A theory for local evaporation (or heat transfer) from rough and smooth surfaces
923 at ground level, *Water Resour. Res.*, 11(4), 543–550, doi:10.1029/WR011i004p00543, 1975.

924 Cao, B., Quan, X., Brown, N., Stewart-Jones, E. and Gruber, S.: GlobSim (v1.0): Deriving
925 meteorological time series for point locations from multiple global reanalyses, *Geosci. Model*
926 *Dev. Discuss.*, (July), 1–29, doi:10.5194/gmd-2019-157, 2019.

927 Chen, B., Luo, S., Lü, S., Yu, Z. and Ma, D.: Effects of the soil freeze-thaw process on the
928 regional climate of the Qinghai-Tibet Plateau, *Clim. Res.*, 59(3), 243–257,
929 doi:10.3354/cr01217, 2014.

930 Chiesa, D. D., Bertoldi, G., Niedrist, G., Obojes, N., Endrizzi, S., Albertson, J. D., Wohlfahrt,
931 G., Hörtnagl, L. and Tappeiner, U.: Modelling changes in grassland hydrological cycling along
932 an elevational gradient in the Alps, *Ecohydrology*, 7(6), 1453–1473, doi:10.1002/eco.1471,
933 2014.

934 Cosenza, P., Guérin, R. and Tabbagh, A.: Relationship between thermal conductivity and water
935 content of soils using numerical modelling, *Eur. J. Soil Sci.*, 54(3), 581–588,
936 doi:10.1046/j.1365-2389.2003.00539.x, 2003.

937 Cullen, N. J. and Conway, J. P.: A 22 month record of surface meteorology and energy balance
938 from the ablation zone of Brewster Glacier, New Zealand, *J. Glaciol.*, 61(229), 931–946,
939 doi:10.3189/2015JG15J004, 2015.

940 Dall’Amico, M., Endrizzi, S., Gruber, S. and Rigon, R.: A robust and energy-conserving model
941 of freezing variably-saturated soil, *Cryosph.*, 5(2), 469–484, doi:10.5194/tc-5-469-2011,
942 2011a.

943 Dall’Amico, M., Endrizzi, S. and Rigon, R.: Snow mapping of an alpine catchment through
944 the hydrological model GEOTop, in *Proceedings Conference Eaux en montagne*, Lyon, pp. 16–
945 17., 2011b.

946 Dall’Amico, M., Endrizzi, S. and Tasin, S.: MYSNOWMAPS: OPERATIVE HIGH-

947 RESOLUTION REAL-TIME SNOW MAPPING, in Proceedings, International Snow Science
948 Workshop, pp. 328–332, Innsbruck, Austria., 2018.

949 Endrizzi, S.: Snow cover modelling at a local and distributed scale over complex terrain,
950 University of Trento., 2007.

951 Endrizzi, S., Gruber, S., Dall’Amico, M. and Rigon, R.: GEOTop 2.0: simulating the combined
952 energy and water balance at and below the land surface accounting for soil freezing, snow
953 cover and terrain effects, *Geosci. Model Dev.*, 7(6), 2831–2857, doi:10.5194/gmd-7-2831-
954 2014, 2014.

955 Engel, M., Notarnicola, C., Endrizzi, S. and Bertoldi, G.: Snow model sensitivity analysis to
956 understand spatial and temporal snow dynamics in a high-elevation catchment, *Hydrol.*
957 *Process.*, 31(23), 4151–4168, doi:10.1002/hyp.11314, 2017.

958 Eugster, W., Rouse, W. R., Pielke Sr, R. A., Mcfadden, J. P., Baldocchi, D. D., Kittel, T. G. F.,
959 Chapin, F. S., Liston, G. E., Vidale, P. L., Vaganov, E. and Chambers, S.: Land-atmosphere
960 energy exchange in Arctic tundra and boreal forest: available data and feedbacks to climate,
961 *Glob. Chang. Biol.*, 6(S1), 84–115, doi:10.1046/j.1365-2486.2000.06015.x, 2000.

962 Favier, V.: One-year measurements of surface heat budget on the ablation zone of Antizana
963 Glacier 15, Ecuadorian Andes, *J. Geophys. Res.*, 109(D18), 1–15, doi:10.1029/2003JD004359,
964 2004.

965 Fiddes, J. and Gruber, S.: TopoSUB: a tool for efficient large area numerical modelling in
966 complex topography at sub-grid scales, *Geosci. Model Dev.*, 5(5), 1245–1257,
967 doi:10.5194/gmd-5-1245-2012, 2012.

968 Fiddes, J., Endrizzi, S. and Gruber, S.: Large-area land surface simulations in heterogeneous
969 terrain driven by global data sets: application to mountain permafrost, *Cryosph.*, 9(1), 411–
970 426, doi:10.5194/tc-9-411-2015, 2015.

971 Ganju, A. and Gusain, H. S.: Six Years Observations and Analysis of Radiation Parameters

972 and Surface Energy Fluxes on Ice Sheet Near ‘Maitri’ Research Station, East Antarctica, Proc.
973 Indian Natl. Sci. Acad., 83(2), 449–460, 2017.

974 Gao, T., Zhang, T., Guo, H., Hu, Y., Shang, J. and Zhang, Y.: Impacts of the active layer on
975 runoff in an upland permafrost basin, northern Tibetan Plateau, edited by J. A. Añel, PLoS
976 One, 13(2), 1–15, doi:10.1371/journal.pone.0192591, 2018.

977 Garratt, J. R.: The atmospheric boundary layer. Cambridge atmospheric and space science
978 series, Cambridge University Press., 1994.

979 Giesen, R. H., Andreassen, L. M., van den Broeke, M. R. and Oerlemans, J.: Comparison of
980 the meteorology and surface energy balance at Storbreen and Midtdalsbreen, two glaciers in
981 southern Norway, Cryosph., 3(1), 57–74, doi:10.5194/tc-3-57-2009, 2009.

982 Gruber, S. and Haeberli, W.: Permafrost in steep bedrock slopes and its temperature-related
983 destabilization following climate change, J. Geophys. Res., 112(F2), 1–10,
984 doi:10.1029/2006JF000547, 2007.

985 Gruber, S., Hoelzle, M. and Haeberli, W.: Permafrost thaw and destabilization of Alpine rock
986 walls in the hot summer of 2003, Geophys. Res. Lett., 31(L13504), 1–4,
987 doi:10.1029/2004GL020051, 2004.

988 Gruber, S., Fleiner, R., Guegan, E., Panday, P., Schmid, M. O., Stumm, D., Wester, P., Zhang,
989 Y. and Zhao, L.: Review article: Inferring permafrost and permafrost thaw in the mountains of
990 the Hindu Kush Himalaya region, Cryosph., 11(1), 81–99, doi:10.5194/tc-11-81-2017, 2017.

991 Gu, L., Yao, J., Hu, Z. and Zhao, L.: Comparison of the surface energy budget between regions
992 of seasonally frozen ground and permafrost on the Tibetan Plateau, Atmos. Res., 153, 553–
993 564, doi:10.1016/j.atmosres.2014.10.012, 2015.

994 Gubler, S.: Measurement Variability and Model Uncertainty in Mountain Permafrost Research,
995 University of Zurich., 2013.

996 Gubler, S., Endrizzi, S., Gruber, S. and Purves, R. S.: Sensitivities and uncertainties of modeled

997 ground temperatures in mountain environments, *Geosci. Model Dev.*, 6(4), 1319–1336,
998 doi:10.5194/gmd-6-1319-2013, 2013.

999 Haerberli, W., Noetzli, J., Arenson, L., Delaloye, R., Gärtner-Roer, I., Gruber, S., Isaksen, K.,
1000 Kneisel, C., Krautblatter, M. and Phillips, M.: Mountain permafrost: development and
1001 challenges of a young research field, *J. Glaciol.*, 56(200), 1043–1058,
1002 doi:10.3189/002214311796406121, 2010.

1003 Harris, C., Davies, M. C. R. and Etzelmüller, B.: The assessment of potential geotechnical
1004 hazards associated with mountain permafrost in a warming global climate, *Permafr. Periglac.*
1005 *Process.*, 12(1), 145–156, doi:10.1002/ppp.376, 2001.

1006 Hasler, A., Geertsema, M., Foord, V., Gruber, S. and Noetzli, J.: The influence of surface
1007 characteristics, topography and continentality on mountain permafrost in British Columbia,
1008 *Cryosph.*, 9(3), 1025–1038, doi:10.5194/tc-9-1025-2015, 2015.

1009 Hingerl, L., Kunstmann, H., Wagner, S., Mauder, M., Bliefernicht, J. and Rigon, R.: Spatio-
1010 temporal variability of water and energy fluxes - a case study for a mesoscale catchment in pre-
1011 alpine environment, *Hydrol. Process.*, 30(21), 3804–3823, doi:10.1002/hyp.10893, 2016.

1012 Hock, R., Rasul, G., Adler, C., Cáceres, B., Gruber, S., Hirabayashi, Y., Jackson, M., Kääb,
1013 A., Kang, S., Kutuzov, S., Milner, A., Molau, U., Morin, S., Orlove, B. and Steltzer, H.: High
1014 Mountain Areas. In: *IPCC Special Report on the Ocean and Cryosphere in a Changing Climate*
1015 [H.-O. Pörtner, D.C. Roberts, V. Masson-Delmotte, P. Zhai, M. Tignor, E. Poloczanska, K.
1016 Mintenbeck, A. Alegría, M. Nicolai, A. Okem, J. Petzold, B. Rama, N.M., 2019.

1017 Hu, G., Zhao, L., Li, R., Wu, X., Wu, T., Zhu, X., Pang, Q., Liu, G. yue, Du, E., Zou, D., Hao,
1018 J. and Li, W.: Simulation of land surface heat fluxes in permafrost regions on the Qinghai-
1019 Tibetan Plateau using CMIP5 models, *Atmos. Res.*, 220, 155–168,
1020 doi:10.1016/j.atmosres.2019.01.006, 2019.

1021 Immerzeel, W. W., van Beek, L. P. H., Konz, M., Shrestha, A. B. and Bierkens, M. F. P.:

1022 Hydrological response to climate change in a glacierized catchment in the Himalayas, *Clim.*
1023 *Change*, 110(3–4), 721–736, doi:10.1007/s10584-011-0143-4, 2012.

1024 Immerzeel, W. W., Wanders, N., Lutz, A. F., Shea, J. M. and Bierkens, M. F. P.: Reconciling
1025 high-altitude precipitation in the upper Indus basin with glacier mass balances and runoff,
1026 *Hydrol. Earth Syst. Sci.*, 19(11), 4673–4687, doi:10.5194/hess-19-4673-2015, 2015.

1027 Isaksen, K., Heggem, E. S. F., Bakkehøi, S., Ødegård, R. S., Eiken, T., Etzelmüller, B. and
1028 Sollid, J. L.: Mountain permafrost and energy balance on Juvvasshøe, southern Norway, in
1029 *Eight International Conference on Permafrost*, vol. 1, edited by M. Phillips, S. Springman, and
1030 L. Arenson, pp. 467–472, Swets & Zeitlinger, Lisse, Zurich, Switzerland., 2003.

1031 Jordan, R. E., Andreas, E. L. and Makshtas, A. P.: Heat budget of snow-covered sea ice at
1032 North Pole 4, *J. Geophys. Res. Ocean.*, 104(C4), 7785–7806, doi:10.1029/1999JC900011,
1033 1999.

1034 Kaser, G., Grosshauser, M. and Marzeion, B.: Contribution potential of glaciers to water
1035 availability in different climate regimes, *Proc. Natl. Acad. Sci.*, 107(47), 20223–20227,
1036 doi:10.1073/pnas.1008162107, 2010.

1037 Kodama, Y., Sato, N., Yabuki, H., Ishii, Y., Nomura, M. and Ohata, T.: Wind direction
1038 dependency of water and energy fluxes and synoptic conditions over a tundra near Tiksi,
1039 Siberia, *Hydrol. Process.*, 21(15), 2028–2037, doi:10.1002/hyp.6712, 2007.

1040 Langer, M., Westermann, S., Muster, S., Piel, K. and Boike, J.: The surface energy balance of
1041 a polygonal tundra site in northern Siberia - Part 2: Winter, *Cryosphere*, 5(2), 509–524,
1042 doi:10.5194/tc-5-509-2011, 2011a.

1043 Langer, M., Westermann, S., Muster, S., Piel, K. and Boike, J.: The surface energy balance of
1044 a polygonal tundra site in northern Siberia – Part 1: Spring to fall, *Cryosph.*, 5(1), 151–171,
1045 doi:10.5194/tc-5-151-2011, 2011b.

1046 Lloyd, C. R., Harding, R. J., Friborg, T. and Aurela, M.: Surface fluxes of heat and water

1047 vapour from sites in the European Arctic, *Theor. Appl. Climatol.*, 70(1–4), 19–33,
1048 doi:10.1007/s007040170003, 2001.

1049 Lone, S. A., Jeelani, G., Deshpande, R. D. and Mukherjee, A.: Stable isotope ($\delta^{18}\text{O}$ and δD)
1050 dynamics of precipitation in a high altitude Himalayan cold desert and its surroundings in Indus
1051 river basin, Ladakh, *Atmos. Res.*, 221(October 2018), 46–57,
1052 doi:10.1016/j.atmosres.2019.01.025, 2019.

1053 Lunardini, V. J.: Heat transfer in cold climates, Van Nostrand Reinhold Company., 1981.

1054 Lutz, A. F., Immerzeel, W. W., Shrestha, A. B. and Bierkens, M. F. P.: Consistent increase in
1055 High Asia's runoff due to increasing glacier melt and precipitation, *Nat. Clim. Chang.*, 4(7),
1056 587–592, doi:10.1038/nclimate2237, 2014.

1057 Lynch, A. H., Chapin, F. S., Hinzman, L. D., Wu, W., Lilly, E., Vourlitis, G. and Kim, E.:
1058 Surface Energy Balance on the Arctic Tundra: Measurements and Models, *J. Clim.*, 12(8),
1059 2585–2606, doi:10.1175/1520-0442(1999)012<2585:SEBOTA>2.0.CO;2, 1999.

1060 MacDonell, S., Kinnard, C., Mölg, T., Nicholson, L. and Abermann, J.: Meteorological drivers
1061 of ablation processes on a cold glacier in the semi-arid Andes of Chile, *Cryosph.*, 7(5), 1513–
1062 1526, doi:10.5194/tc-7-1513-2013, 2013.

1063 Mair, E., Leitinger, G., Della Chiesa, S., Niedrist, G., Tappeiner, U. and Bertoldi, G.: A simple
1064 method to combine snow height and meteorological observations to estimate winter
1065 precipitation at sub-daily resolution, *Hydrol. Sci. J.*, 61(11), 2050–2060,
1066 doi:10.1080/02626667.2015.1081203, 2016.

1067 Marshall, S. J.: Meltwater run-off from Haig Glacier, Canadian Rocky Mountains, 2002–2013,
1068 *Hydrol. Earth Syst. Sci.*, 18(12), 5181–5200, doi:10.5194/hess-18-5181-2014, 2014.

1069 Martin, E. and Lejeune, Y.: Turbulent fluxes above the snow surface, *Ann. Glaciol.*, 26(1),
1070 179–183, doi:10.3189/1998AoG26-1-179-183, 1998.

1071 Mauder, M., Genzel, S., Fu, J., Kiese, R., Soltani, M., Steinbrecher, R., Zeeman, M., Banerjee,

1072 T., De Roo, F. and Kunstmann, H.: Evaluation of energy balance closure adjustment methods
1073 by independent evapotranspiration estimates from lysimeters and hydrological simulations,
1074 *Hydrol. Process.*, 32(1), 39–50, doi:10.1002/hyp.11397, 2018.

1075 McBean, G. A. and Miyake, M.: Turbulent transfer mechanisms in the atmospheric surface
1076 layer, *Q. J. R. Meteorol. Soc.*, 98(416), 383–398, doi:10.1002/qj.49709841610, 1972.

1077 Mittaz, C., Hoelzle, M. and Haeberli, W.: First results and interpretation of energy-flux
1078 measurements over Alpine permafrost, *Ann. Glaciol.*, 31, 275–280,
1079 doi:10.3189/172756400781820363, 2000.

1080 Mölg, T.: Ablation and associated energy balance of a horizontal glacier surface on
1081 Kilimanjaro, *J. Geophys. Res.*, 109(D16), D16104, doi:10.1029/2003JD004338, 2004.

1082 Mölg, T., Maussion, F., Yang, W. and Scherer, D.: The footprint of Asian monsoon dynamics
1083 in the mass and energy balance of a Tibetan glacier, *Cryosph.*, 6(6), 1445–1461,
1084 doi:10.5194/tc-6-1445-2012, 2012.

1085 Monin, A. S. and Obukhov, A. M.: Basic laws of turbulent mixing in the atmosphere near the
1086 ground, *Tr. Akad. Nauk SSSR Geofiz. Inst*, 24(151), 163–187, 1954.

1087 Mu, C., Li, L., Wu, X., Zhang, F., Jia, L., Zhao, Q. and Zhang, T.: Greenhouse gas released
1088 from the deep permafrost in the northern Qinghai-Tibetan Plateau, *Sci. Rep.*, 8(1), 1–9,
1089 doi:10.1038/s41598-018-22530-3, 2018.

1090 Nash, J. E. and Sutcliffe, J. V.: River flow forecasting through conceptual models part I — A
1091 discussion of principles, *J. Hydrol.*, 10(3), 282–290, doi:10.1016/0022-1694(70)90255-6,
1092 1970.

1093 Nicholson, L. I., Prinz, R., Mölg, T. and Kaser, G.: Micrometeorological conditions and surface
1094 mass and energy fluxes on Lewis Glacier, Mt Kenya, in relation to other tropical glaciers,
1095 *Cryosph.*, 7(4), 1205–1225, doi:10.5194/tc-7-1205-2013, 2013.

1096 Oerlemans, J. and Klok, E. J.: Energy Balance of a Glacier Surface: Analysis of Automatic

1097 Weather Station Data from the Morteratschgletscher, Switzerland, Arctic, Antarct. Alp. Res.,
1098 34(4), 477–485, doi:10.1080/15230430.2002.12003519, 2002.

1099 Ohmura, A.: Climate and energy balance on the arctic tundra, *J. Climatol.*, 2(1), 65–84,
1100 doi:10.1002/joc.3370020106, 1982.

1101 Ohmura, A.: Comparative energy balance study for arctic tundra, sea surface glaciers and
1102 boreal forests, *GeoJournal*, 8(3), 221–228, doi:10.1007/BF00446471, 1984.

1103 Oke, T. R.: *Boundary Layer Climates*, Routledge., 2002.

1104 Pandey, P.: Inventory of rock glaciers in Himachal Himalaya, India using high-resolution
1105 Google Earth imagery, *Geomorphology*, 340, 103–115, doi:10.1016/j.geomorph.2019.05.001,
1106 2019.

1107 Pellicciotti, F., Helbing, J., Rivera, A., Favier, V., Corripio, J., Araos, J., Sicart, J.-E. and
1108 Carenzo, M.: A study of the energy balance and melt regime on Juncal Norte Glacier, semi-
1109 arid Andes of central Chile, using melt models of different complexity, *Hydrol. Process.*,
1110 22(19), 3980–3997, doi:10.1002/hyp.7085, 2008.

1111 PERMOS: Permafrost in Switzerland 2014/2015 to 2017/2018. Noetzi, J., Pellet, C. and Staub,
1112 B. (eds.), *Glaciological Report Permafrost No. 16-19 of the Cryospheric Commission of the*
1113 *Swiss Academy of Sciences*, 104 pp., 2019.

1114 Pogliotti, P.: *Influence of snow cover on MAGST over complex morphologies in mountain*
1115 *permafrost regions*, University of Torino, Torino., 2011.

1116 Pritchard, H. D.: Asia’s shrinking glaciers protect large populations from drought stress,
1117 *Nature*, 569(7758), 649–654, doi:10.1038/s41586-019-1240-1, 2019.

1118 R Core Team: *R: A Language and Environment for Statistical Computing*, [online] Available
1119 from: <https://www.r-project.org/>, 2016.

1120 Rasmussen, R., Baker, B., Kochendorfer, J., Meyers, T., Landolt, S., Fischer, A. P., Black, J.,
1121 Thériault, J. M., Kucera, P., Gochis, D., Smith, C., Nitu, R., Hall, M., Ikeda, K. and Gutmann,

1122 E.: How Well Are We Measuring Snow: The NOAA/FAA/NCAR Winter Precipitation Test
1123 Bed, *Bull. Am. Meteorol. Soc.*, 93(6), 811–829, doi:10.1175/BAMS-D-11-00052.1, 2012.

1124 Rastogi, S. P. and Narayan, S.: Permafrost areas in Tso Kar Basin, in *Symposium for Snow,*
1125 *Ice and Glaciers*, March 1999, pp. 315–319, Geological Survey of India Special Publication
1126 53., 1999.

1127 Rigon, R., Bertoldi, G. and Over, T. M.: GEOTop: A Distributed Hydrological Model with
1128 Coupled Water and Energy Budgets, *J. Hydrometeorol.*, 7(3), 371–388,
1129 doi:10.1175/JHM497.1, 2006.

1130 Roberts, K. E., Lamoureux, S. F., Kyser, T. K., Muir, D. C. G., Lafrenière, M. J., Iqaluk, D.,
1131 Pieńkowski, A. J. and Normandeau, A.: Climate and permafrost effects on the chemistry and
1132 ecosystems of High Arctic Lakes, *Sci. Rep.*, 7(1), 1–8, doi:10.1038/s41598-017-13658-9,
1133 2017.

1134 Roesch, A., Wild, M., Pinker, R. and Ohmura, A.: Comparison of spectral surface albedos and
1135 their impact on the general circulation model simulated surface climate, *J. Geophys. Res.*,
1136 107(D14), 4221, doi:10.1029/2001JD000809, 2002.

1137 Salzmann, N., Nötzli, J., Hauck, C., Gruber, S., Hoelzle, M. and Haeberli, W.: Ground surface
1138 temperature scenarios in complex high-mountain topography based on regional climate model
1139 results, *J. Geophys. Res.*, 112(F2), 1–10, doi:10.1029/2006JF000527, 2007.

1140 Schmid, M.-O., Baral, P., Gruber, S., Shahi, S., Shrestha, T., Stumm, D. and Wester, P.:
1141 Assessment of permafrost distribution maps in the Hindu Kush Himalayan region using rock
1142 glaciers mapped in Google Earth, *Cryosph.*, 9(6), 2089–2099, doi:10.5194/tc-9-2089-2015,
1143 2015.

1144 Sellers, W. D.: *Physical climatology*, The University of Chicago Press., 1965.

1145 Singh, N., Singhal, M., Chhikara, S., Karakoti, I., Chauhan, P. and Dobhal, D. P.: Radiation
1146 and energy balance dynamics over a rapidly receding glacier in the central Himalaya, *Int. J.*

1147 Climatol., 40(1), 400–420, doi:10.1002/joc.6218, 2020.

1148 Soltani, M., Laux, P., Mauder, M. and Kunstmann, H.: Inverse distributed modelling of
1149 streamflow and turbulent fluxes: A sensitivity and uncertainty analysis coupled with automatic
1150 optimization, *J. Hydrol.*, 571, 856–872, doi:10.1016/j.jhydrol.2019.02.033, 2019.

1151 Stiegler, C., Johansson, M., Christensen, T. R., Mastepanov, M. and Lindroth, A.: Tundra
1152 permafrost thaw causes significant shifts in energy partitioning, *Tellus B Chem. Phys.*
1153 *Meteorol.*, 68(1), 1–11, doi:10.3402/tellusb.v68.30467, 2016.

1154 Stocker-Mittaz, C.: Permafrost Distribution Modeling Based on Energy Balance Data,
1155 University of Zurich, Switzerland., 2002.

1156 Stull, R. B.: An Introduction to Boundary Layer Meteorology, Springer Netherlands,
1157 Dordrecht., 1988.

1158 Thakur, V. C.: Regional framework and geodynamic evolution of the Indus-Tsangpo suture
1159 zone in the Ladakh Himalayas, *Trans. R. Soc. Edinb. Earth Sci.*, 72(2), 89–97,
1160 doi:10.1017/S0263593300009925, 1981.

1161 Thayyen, R. J.: Ground ice melt in the catchment runoff in the Himalayan cold-arid system, in
1162 IGS Symposium on Glaciology in High-Mountain Asia, Kathmandu, Nepal, 1-6 March 2015,
1163 Kathmandu, Nepal., 2015.

1164 Thayyen, R. J.: Hydrology of the Cold-Arid Himalaya, in *Himalayan Weather and Climate and
1165 their Impact on the Environment*, pp. 399–417, Springer International Publishing, Cham., 2020.

1166 Thayyen, R. J. and Dimri, A. P.: Factors controlling Slope Environmental Lapse Rate (SELR)
1167 of temperature in the monsoon and cold-arid glacio-hydrological regimes of the Himalaya,
1168 *Cryosph. Discuss.*, 8(6), 5645–5686, doi:10.5194/tcd-8-5645-2014, 2014.

1169 Thayyen, R. J. and Gergan, J. T.: Role of glaciers in watershed hydrology: a preliminary study
1170 of a “Himalayan catchment,” *Cryosph.*, 4(1), 115–128, doi:10.5194/tc-4-115-2010, 2010.

1171 Thayyen, R. J., Dimri, A. P., Kumar, P. and Agnihotri, G.: Study of cloudburst and flash floods

1172 around Leh, India, during August 4–6, 2010, *Nat. Hazards*, 65(3), 2175–2204,
1173 doi:10.1007/s11069-012-0464-2, 2013.

1174 Thayyen, R. J., Rai, S. P. and Goel, M. K.: Glaciological studies of Phuche glacier, Ladakh
1175 Range., 2015.

1176 Wang, G., Li, Y., Wu, Q. and Wang, Y.: Impacts of permafrost changes on alpine ecosystem
1177 in Qinghai-Tibet Plateau, *Sci. China Ser. D Earth Sci.*, 49(11), 1156–1169,
1178 doi:10.1007/s11430-006-1156-0, 2006.

1179 Wang, X., Chen, R. and Yang, Y.: Effects of Permafrost Degradation on the Hydrological
1180 Regime in the Source Regions of the Yangtze and Yellow Rivers, China, *Water*, 9(11), 1–13,
1181 doi:10.3390/w9110897, 2017.

1182 Wani, J. M., Thayyen, R. J., Gruber, S., Ojha, C. S. P. and Stumm, D.: Single-year thermal
1183 regime and inferred permafrost occurrence in the upper Ganglass catchment of the cold-arid
1184 Himalaya, Ladakh, India, *Sci. Total Environ.*, 703, doi:10.1016/j.scitotenv.2019.134631, 2020.

1185 Westermann, S., Lüers, J., Langer, M., Piel, K. and Boike, J.: The annual surface energy budget
1186 of a high-arctic permafrost site on Svalbard, Norway, *Cryosph.*, 3(2), 245–263, doi:10.5194/tc-
1187 3-245-2009, 2009.

1188 Wickham, H.: *ggplot2: Elegant Graphics for Data Analysis*, [online] Available from:
1189 <https://ggplot2.tidyverse.org>, 2016.

1190 Wickham, H.: *tidyverse: Easily Install and Load the “Tidyverse”*, [online] Available from:
1191 <https://cran.r-project.org/package=tidyverse>, 2017.

1192 Wickham, H. and Francois, R.: *dplyr: A Grammar of Data Manipulation*, [online] Available
1193 from: <https://cran.r-project.org/package=dplyr>, 2016.

1194 Wilke, C. O.: *cowplot: Streamlined Plot Theme and Plot Annotations for “ggplot2,”* [online]
1195 Available from: <https://cran.r-project.org/package=cowplot>, 2019.

1196 Woo, M.-K., Kane, D. L., Carey, S. K. and Yang, D.: Progress in permafrost hydrology in the

1197 new millennium, *Permafr. Periglac. Process.*, 19(2), 237–254, doi:10.1002/ppp.613, 2008.

1198 Wünnemann, B., Reinhardt, C., Kotlia, B. S. and Riedel, F.: Observations on the relationship
1199 between lake formation, permafrost activity and lithalsa development during the last 20 000
1200 years in the Tso Kar basin, Ladakh, India, *Permafr. Periglac. Process.*, 19(4), 341–358,
1201 doi:10.1002/ppp.631, 2008.

1202 Xia, Z.: Simulation of the Bare Soil Surface Energy Balance at the Tongyu Reference Site in
1203 Semiarid Area of North China, *Atmos. Ocean. Sci. Lett.*, 3(6), 330–335,
1204 doi:10.1080/16742834.2010.11446892, 2010.

1205 Yang, D., Goodison, B. E., Metcalfe, J. R., Louie, P., Leavesley, G., Emerson, D., Hanson, C.
1206 L., Golubev, V. S., Elomaa, E., Gunther, T., Pangburn, T., Kang, E. and Milkovic, J.:
1207 Quantification of precipitation measurement discontinuity induced by wind shields on national
1208 gauges, *Water Resour. Res.*, 35(2), 491–508, doi:10.1029/1998WR900042, 1999.

1209 Yao, J., Zhao, L., Ding, Y., Gu, L., Jiao, K., Qiao, Y. and Wang, Y.: The surface energy budget
1210 and evapotranspiration in the Tanggula region on the Tibetan Plateau, *Cold Reg. Sci. Technol.*,
1211 52(3), 326–340, doi:10.1016/j.coldregions.2007.04.001, 2008.

1212 Yao, J., Zhao, L., Gu, L., Qiao, Y. and Jiao, K.: The surface energy budget in the permafrost
1213 region of the Tibetan Plateau, *Atmos. Res.*, 102(4), 394–407,
1214 doi:10.1016/j.atmosres.2011.09.001, 2011.

1215 Yao, J., Gu, L., Yang, C., Chen, H., Wang, J., Ding, Y., Li, R., Zhao, L., Xiao, Y., Qiao, Y.,
1216 Shi, J. and Chen, C.: Estimation of surface energy fluxes in the permafrost region of the Tibetan
1217 Plateau based on situ measurements and the <sc>SEBS</sc> model, *Int. J. Climatol.*,
1218 joc.6551, doi:10.1002/joc.6551, 2020.

1219 Ye, Z. and Pielke, R. A.: Atmospheric Parameterization of Evaporation from Non-Plant-
1220 covered Surfaces, *J. Appl. Meteorol.*, 32(7), 1248–1258, doi:10.1175/1520-
1221 0450(1993)032<1248:APOEFN>2.0.CO;2, 1993.

- 1222 Zanotti, F., Endrizzi, S., Bertoldi, G. and Rigon, R.: The GEOTOP snow module, *Hydrol.*
1223 *Process.*, 18(18), 3667–3679, doi:10.1002/hyp.5794, 2004.
- 1224 Zhang, G., Kang, S., Fujita, K., Huintjes, E., Xu, J., Yamazaki, T., Haginoya, S., Wei, Y.,
1225 Scherer, D., Schneider, C. and Yao, T.: Energy and mass balance of Zhadang glacier surface,
1226 central Tibetan Plateau, *J. Glaciol.*, 59(213), 137–148, doi:10.3189/2013JoG12J152, 2013.
- 1227 Zhao, L., Cheng, G., Li, S., Zhao, X. and Wang, S.: Thawing and freezing processes of active
1228 layer in Wudaoliang region of Tibetan Plateau, *Chinese Sci. Bull.*, 45(23), 2181–2187,
1229 doi:10.1007/BF02886326, 2000.
- 1230 Zhu, M., Yao, T., Yang, W., Maussion, F., Huintjes, E. and Li, S.: Energy- and mass-balance
1231 comparison between Zhadang and Parlung No. 4 glaciers on the Tibetan Plateau, *J. Glaciol.*,
1232 61(227), 595–607, doi:10.3189/2015JoG14J206, 2015.
1233